

## N O T I C E

THIS DOCUMENT HAS BEEN REPRODUCED FROM  
MICROFICHE. ALTHOUGH IT IS RECOGNIZED THAT  
CERTAIN PORTIONS ARE ILLEGIBLE, IT IS BEING RELEASED  
IN THE INTEREST OF MAKING AVAILABLE AS MUCH  
INFORMATION AS POSSIBLE

NASA CONTRACTOR REPORT 159146

FINAL REPORT  
STUDY OF A

# STEREO-ELECTRO-OPTICAL TRACKER SYSTEM

FOR  
THE MEASUREMENT OF MODEL DEFORMATIONS  
AT THE NATIONAL TRANSONIC FACILITY

RICHARD J. HERTEL

ITT AEROSPACE/OPTICAL DIVISION  
FORT WAYNE, INDIANA 46803

CONTRACT NAS1-15629  
OCTOBER 1979

(NASA-CR-159146) STUDY OF A STEREO  
ELECTRO-OPTICAL TRACKER SYSTEM FOR THE  
MEASUREMENT OF MODEL DEFORMATIONS AT THE  
NATIONAL TRANSONIC FACILITY Final Report  
(ITT Aerospace/Optical Div.) 82 p

N80-10476

*MC. Perfor. Ac 1*

Unclas  
G3/35 45845



National Aeronautics and  
Space Administration

Langley Research Center  
Hampton, Virginia 23665  
AC 804 827-3965



1. Report No. 159146		2. Government Accession No.		3. Recipient's Catalog No.	
4. Title and Subtitle Study of a Stereo Electro-Optical Tracker System for Measurement of Model Aerelastic Deformations at the National Transonic Facility				5. Report Date 25 October 1979	
				6. Performing Organization Code	
7. Author(s) Richard J. Hertel				8. Performing Organization Report No.	
9. Performing Organization Name and Address ITT Aerospace/Optical Division 3700 East Pontiac Street Fort Wayne, IN 46803				10. Work Unit No.	
				11. Contract or Grant No. NASI-15629	
12. Sponsoring Agency Name and Address  National Aeronautics and Space Administration Langley Research Center Hampton, VA				13. Type of Report and Period Covered Contractor Report	
				14. Army Project No.	
15. Supplementary Notes					
16. Abstract  This study and report provides an analytical and experimental basis to support the concept of a stereo electro-optical tracker system to measure multiple targets attached to aircraft models in the wind tunnel at the National Transonic Facility.  The study showed that given a 0.8m x 1.0m field of view and 150 $\mu$ m precision at the model, 5-50 point illuminated targets can be acquired and tracked. Furthermore, the intensities of the targets, tunnel background illumination, and system data rates are within reasonable bounds. A demonstration showed a time scaled simulation of a five target tracker operating at the expected electro-optical signal-to-noise ratio and desired precision. The analysis and demonstration also showed that targets vibrating at frequencies of 8, 50, and 200 Hz can be located and measured.					
17. Key Words (Suggested by Author(s)) Model Deformation Instrumentation Displacement Measurement Systems Stereographic Measurement Electro-Optical Tracker			18. Distribution Statement  Unclassified Unlimited Distribution		
19. Security Classif. (of this report) Unclassified	20. Security Classif. (of this page) Unclassified	21. No. of Pages 79	22. Price*		

## TABLE OF CONTENTS

<u>Paragraph No.</u>	<u>Title</u>	<u>Page</u>
1.0	SUMMARY.....	1
2.0	SYSTEM DESCRIPTION.....	3
2.1	Tunnel Installation.....	3
2.2	System Operation.....	8
2.2.1	Target Acquisition.....	8
2.2.2	Target Tracking.....	14
2.2.3	System Calibration.....	20
2.3	System Computer.....	21
3.0	ANALYSIS AND EXPERIMENTS.....	22
3.1	Optics.....	22
3.2	Targets.....	24
3.2.1	Point Versus Finite Sized Targets.....	25
3.2.2	Active Versus Passive Targets.....	26
3.2.3	Target Contrast.....	28
3.2.4	Angular Distribution of the Target Light.....	32
3.3	Target Dynamics.....	32
3.4	Image Dissector Camera.....	34
3.4.1	Image Dissector Camera.....	34
3.4.2	Digital Interface Unit.....	34
3.5	Tracker Characteristics.....	35
3.5.1	Error Detector.....	35
3.5.2	Noise Equivalent Position.....	38
3.5.3	Measurement Cycles for Null Convergence.....	38
3.6	System Precision Accuracy.....	42
3.6.1	Camera and Camera Lens Effects upon System Precision.....	43
3.6.2	Target Dynamics Motion Effects upon System Precision.....	46
3.6.3	Camera Dynamic Motion Effects upon System Precision.....	51
3.6.4	Seeing Conditions.....	51
3.7	Use of Tracker Cameras for TV Viewing of the Tunnel Interior.....	52
3.8	Demonstration.....	55
3.8.1	Field of View.....	55
3.8.2	Targets.....	55
3.8.3	Target Acquisition.....	55
3.8.4	Track and Measurement.....	57
3.8.5	Target Dynamic Simulation.....	57
4.0	CONCLUSIONS AND RECOMMENDATIONS.....	60
4.1	Credits.....	61
APPENDIX	The Image Dissector as an Optical Tracker.....	63

# LIST OF ILLUSTRATIONS

<u>Figure No.</u>	<u>Title</u>	<u>Page</u>
1	Side View of the Optical Field of View and Coordinate Systems in the Plane $Y_0 = 400$ mm.....	4
2	Top View of the Optical Field of View and Coordinate Systems in the Plane $Y_0 = 1352$ mm and Zero Angle of Attack.....	5
3	Camera Installation at the Test Section Wall.....	7
4	System Electrical Block Diagram.....	9
5	Program TBOSS Flow Chart.....	10
6	Point Tracker Operating Principle.....	15
7	Capture Range for a $200 \times 200 \mu\text{m}$ Image Dissector Aperture and a $35 \mu\text{m}$ Point Spread Function.....	17
8	Tracker Function Timing Diagram.....	19
9	Camera Image Formats and Lens Focal Lengths for Three Sizes of Image Dissectors.....	23
10	Two Examples of Finite Targets.....	25
11	Finite Targets View at Large Angles.....	26
12	Target Intensity Versus Background Luminance.....	30
13	LED Relative Intensity Versus Wavelength.....	31
14	Normalized Error Detector Curve Showing Brightness Unbalance Versus Position Effect.....	36
15	Slope of the Normalized Error Detector Curve.....	37
16	Slope Changes in the Normalized Error Curve for Changes in Focal Plane Position.....	39
17	Noise Equivalent Position Versus Signal-to-Noise Ratio.....	40
18	Cycles to Converge to Null Versus Offset from Null and Loop Gain.....	41
19	10X Magnified Camera Deflection Distortion for a Camera Using $25 \text{ mm}$ Image Dissector Tube Having a $200 \mu\text{m}$ Aperture.....	44

## LIST OF ILLUSTRATIONS (Cont)

<u>Figure No.</u>	<u>Title</u>	<u>Page</u>
20	Vibration Amplitude Versus Frequency Spectrum for Some of the Possible Vibration Modes of the Wind Tunnel Model.....	47
21	Normalized Amplitude Response Versus Number of Targets Reduced Number of Cycles Assumes 2X more Light.....	50
22	Refraction at Test Section Window.....	53
23	Demonstration Test Pattern.....	56
24	Comparison Between Timing Diagram of Stereo Electro-Optical Tracker System and Laboratory Demonstration System.....	58

## LIST OF TABLES

<u>Table No.</u>	<u>Title</u>	<u>Page</u>
1	Target Vibration at the Model and at the Camera....	33
2	Comparison of Stereo Electro-Optical Tracker System Time Scale with the Demonstration System Time Scale.....	57
3	Vibration Simulation Frequencies and Amplitudes....	59

STUDY OF A STEREO-ELECTRO-OPTICAL TRACKER SYSTEM  
FOR THE MEASUREMENT OF MODEL AEROELASTIC DEFORMATIONS  
AT THE NATIONAL TRANSONIC FACILITY

Richard J. Hertel  
ITT Aerospace/Optical Division

1.0 SUMMARY

This study examined an electro-optical method to measure the aeroelastic deformations of wind tunnel models. The system studied is an electronic version of the photogrammetry method described by Brooks and Beamish.<sup>1</sup> In place of the film, its processing and measurement, an electronic camera system is used. Brooks and Beamish measured the recorded image positions of white target dots emplaced in the model. The electronic camera system does the same task in real time. It measures the coordinates of targets focused onto its photosensitive areas.

This study shows the electronic camera system is capable of locating, measuring, and following the positions of 5 to 50 targets attached to the model at measuring rates up to 5000 targets per second. The targets must be either sources or efficient reflectors of light.

This study analyzed, modeled, and measured the multi-target tracking performance of one of the two electronic cameras comprising the stereo pair. Although the conditions used for this study were those estimated to exist in the wind tunnel at the National Transonic Facility, NASA Langley, Langley, Virginia, it is emphasized that a system of this type has broader application. This system can be used in other wind tunnels where the environmental and vibrational conditions are less severe than NTF. This system can in fact be used for a rather wide range of three dimensional surface contour and displacement problems.

This study considered the properties of the targets at the model, the camera optics, target illumination, number of targets, acquisition time, target velocities and accelerations, tracker performance, and other factors affecting the measurement accuracy of target positions.

Stereophotogrammetry has been tested at Langley Research Center as a means of measuring model deformations. Consideration of stereographic transformation was not included in this study inasmuch as the same or similar techniques used in the Langley tests will be applied when using the electro-optical system.

The results of the study are presented here in terms which describe the eventual measuring system; its organization, installation, and operation. A baseline system design is given with comments regarding

---

<sup>1</sup>Measurement of Model Aeroelastic Deformations in the Wind Tunnel at Transonic Speeds Using Stereophotogrammetry, J.D. Brooks and J.K. Beamish, NASA Technical Paper 1010, Oct. 77.

alternatives. Some areas of technical uncertainty remain and these are noted. An analytical and experimental section contains the information needed to support the baseline design and provides the basis for choosing among design alternatives. This report also describes the experiments and the demonstration, conducted at ITT-Aerospace/Optical Division, used to support the analytical work, to demonstrate feasibility of concepts, and to show working software and hardware.



## 2.0

### SYSTEM DESCRIPTION

The system design described in this section is a conceptual one. Most features have only been treated analytically. Some features have been modeled in hardware, and in a few cases experiments have been performed to gather supporting data.

The system described here assumes the use of small, self-luminous targets attached to the model. The targets are viewed by two electronic cameras located in the plenum of the wind tunnel behind optical ports in the test section wall. Operating modes provide for system calibration, target acquisition, target tracking and position measurement. Software dialog with an operator is used to select the system modes. Tunnel supervisory control is expected to identify when valid data logging conditions exist. This system then responds to an external command and records target positions while the model angle of attack is slowly varied. The recorded position information is analyzed later, off line, by the experimenter to extract the three dimensional target motions from the two camera stereo-optical data. Provision is made for a limited amount of quick look examination of the test data. Camera installation and siting are important considerations in the estimated system precision and accuracy.

## 2.1

### Tunnel Installation

Figures 1 and 2 show the general arrangement of an aircraft model, electronic cameras, camera fields of view and coordinate systems used to relate three dimensional model coordinates to two dimensional image plane coordinates.

The aircraft model is supported by the sting and is located along the center line of the tunnel. The model is movable in pitch angle,  $-11^{\circ}$  to  $+19^{\circ}$ , about a center of rotation located within the model. The model space coordinate system is designated (x", y", z") and has its origin at the center of rotation. The model support is made as rigid as possible but it does still bend and vibrate. The bending of the sting with a model attached gives rise to rigid body motions of  $\pm 0.5$  degree amplitude in pitch, roll, and yaw about the center of rotation at frequencies of 8 to 50 Hz. Furthermore, the first bending mode vibrations of the model wing are expected to fall in the range of 25 mm peak-to-peak at 20 Hz to 2.5 mm peak-to-peak at 200 Hz.

The targets are sources of light, less than 500  $\mu$ m diameter and flush with the surface of the model. The targets are either light emitting diodes (LEDs) or the polished end of a fiber optic light pipe. The electrical power input to each target is 100 mW for the LEDs. The fiber optic targets require greater power; depending upon fiber and coupling losses. The targets emit light in all directions, and at angles as great as  $75^{\circ}$  to the normal of the target. All targets must be within the fields of view of both cameras. These and other properties of targets having great importance to system operation are discussed further in Sections 3.2, 3.3, and 3.6.

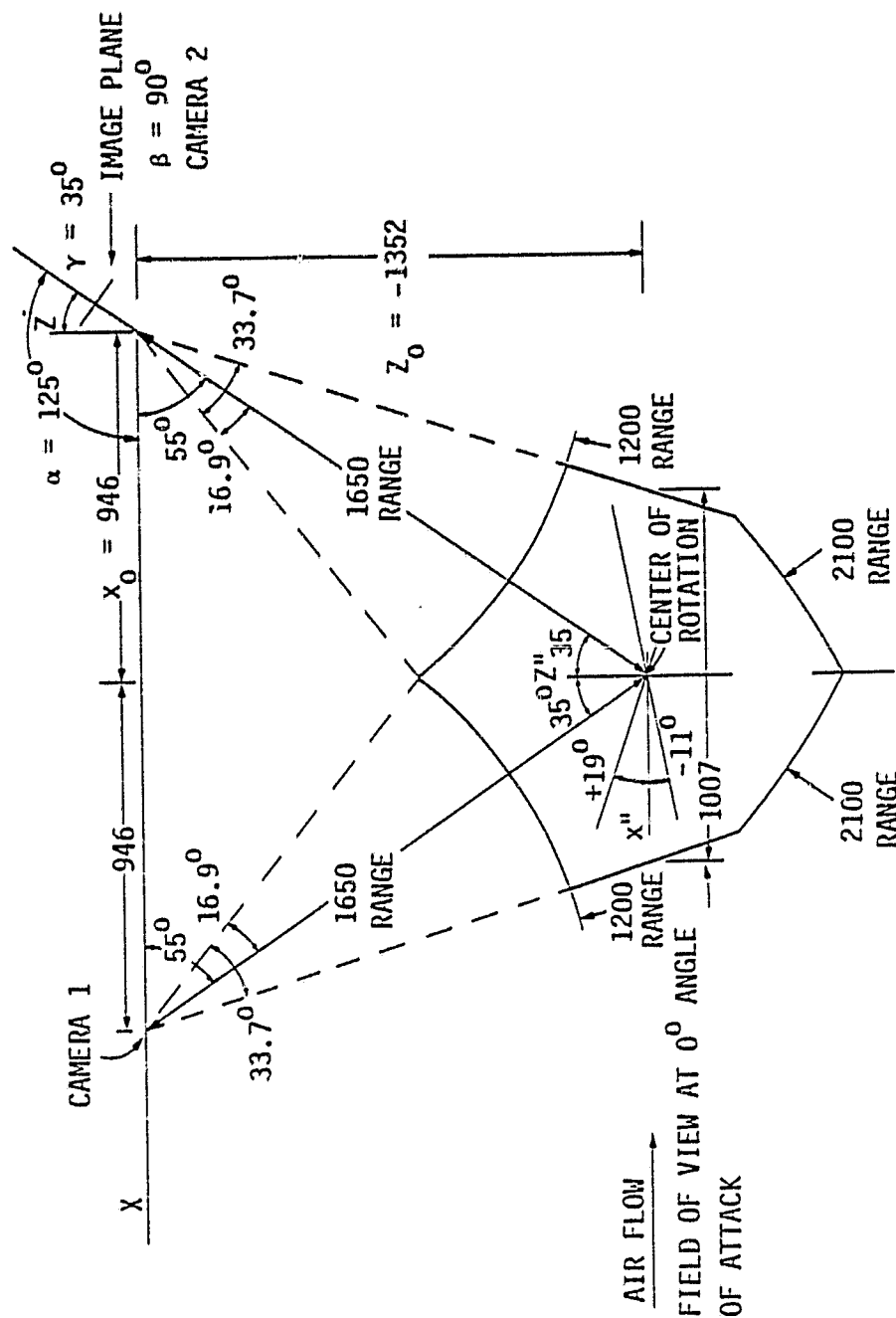


Figure 1. Side View of the Optical Field of View and Coordinate Systems in the Plane  $Y_0 = 400$  mm. (All dimensions in mm)

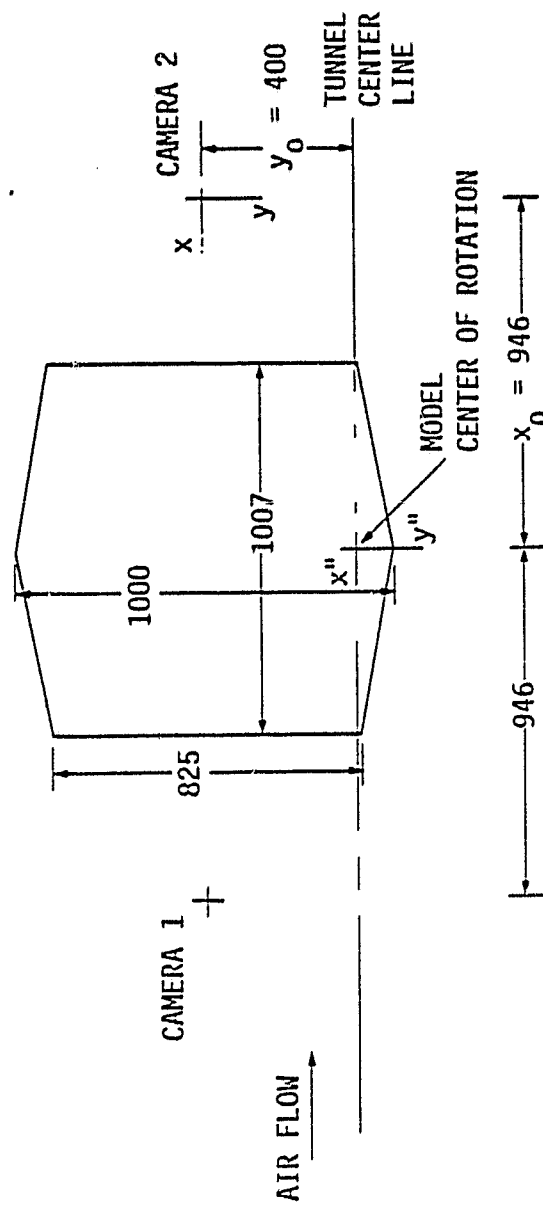


Figure 2. Top View of the Optical Field of View and Coordinate Systems in the Plane  $X_0 = 1352$  mm and Zero Angle of Attack. (All dimensions in mm)

There are two image dissector cameras used in this tracker system. Figures 1 and 2 show these cameras located 400 mm off the center line of the model, at positions upstream and downstream of the model. Camera locations for models having wing spans totally inside the field of view are along the center line of the tunnel, again, upstream and downstream of the model. In Figures 1 and 2, the cameras lines of sight are aimed at a common point located at  $y'' = -400$  mm. The camera pointing angles are  $(\alpha, \beta, \gamma) = (125^\circ, 90^\circ, 35^\circ)$  as shown in the figure. For the center line located cameras, the aim point is the center of rotation.

The system field of view is 800 by 1000 mm at the model for zero degree angle of attack and 1650 mm camera to model range. Figure 2 illustrates an off center line camera installation. The field of view covers the fuselage and one wing of a 1.6 to 1.8 m wing span model. The boundaries of the field of view volume are set by the  $34^\circ \times 34^\circ$  angular field of view of the cameras and the  $1650 \pm 450$  mm depth of focus of the camera optics. Greater depth of focus can be obtained by increasing the  $f$  number of the lens at the expense of increased target illumination power for the same data rates. The field of view can be changed by using a different focal length camera lens. A shorter focal length lens gives a wider field of view and greater depth of focus at the expense of measurement precision at the model. A longer focal length lens has the opposite effect. Carried to an extreme, very short focal length lenses will have greater distortion while very long focal length lenses may have large  $f$  numbers. Section 3.1 on optics discusses these considerations in greater detail.

Each camera head, camera optics, and associated electronics are located inside temperature controlled pressure vessel. A vessel isolates the camera from the wide range of temperature and pressure conditions in the tunnel. The pressure vessel has a 10 mm thick optical quality window at one end. This window withstands the static tunnel pressure. A second optical quality window in the wall of the tunnel test section isolates the pressure vessel from the direct tunnel flow. A sketch of this arrangement is shown in Figure 3.

The proper mounting of the cameras in the pressure vessel and the pressure vessel in the wind tunnel are important considerations. The mounting must minimize changes in the camera-to-model vector due to vibration or temperature. The mounting must also allow for temperature control of the pressure vessel.

Mounting point temperatures can range from  $-195^\circ\text{C}$  to  $95^\circ\text{C}$  making both heating and cooling necessary. The camera and electronics present a 10-12 watt heat load. A satisfactory mounting is just as important as the proper target characteristics. While mounting details are outside the scope of this study, Section 3.6 discusses the precision and accuracy consequences of variations in the camera to model vector.

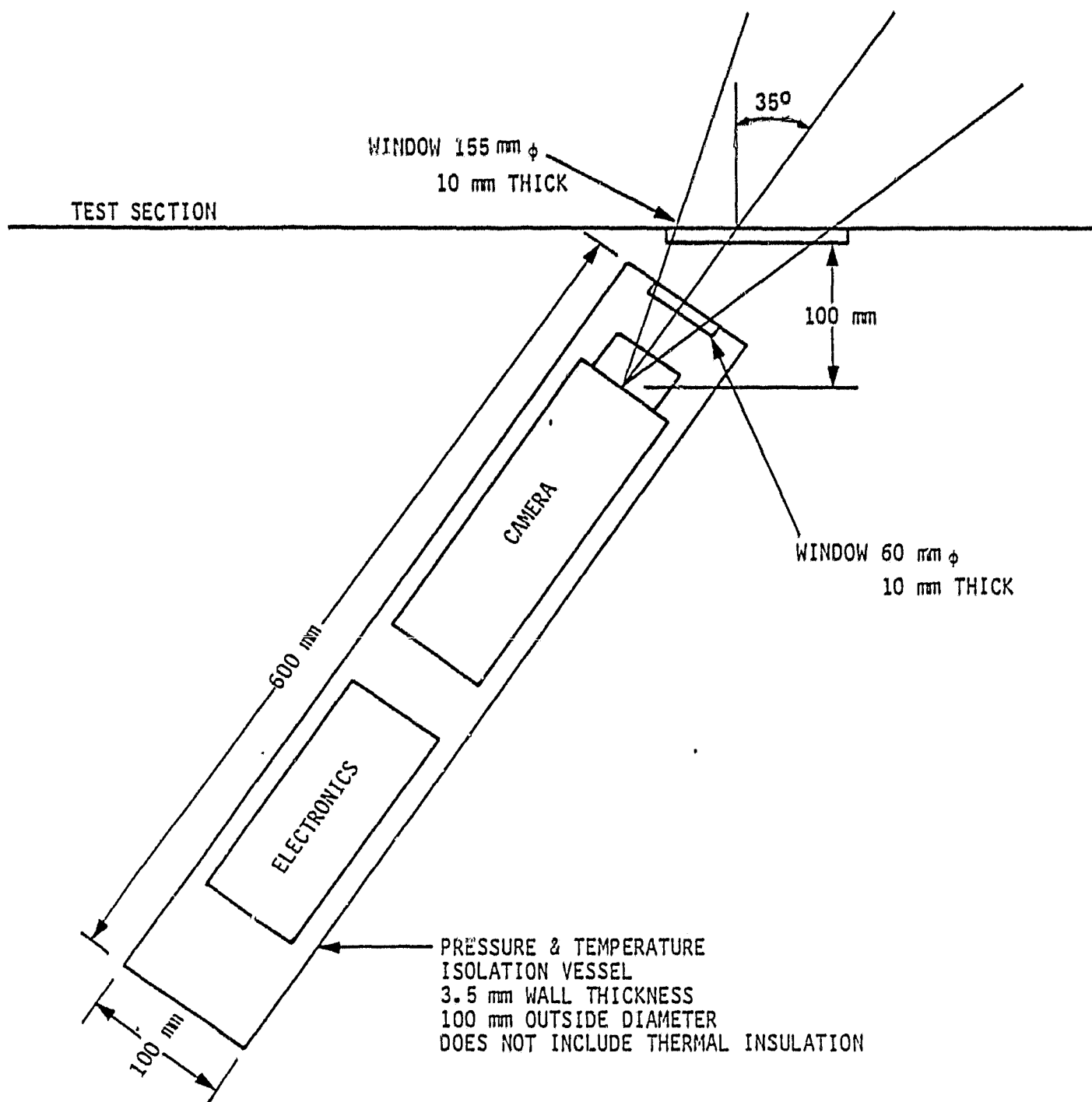


Figure 3. Camera Installation at the Test Section Wall

## 2.2 System Operation

The system hardware is intended to operate upon the command of the system computer. Figure 4 shows a block diagram of the stereo-electro optical tracker system and the interface with the tracker system computer. Each camera\* uses a 16 bit, duplex, I/O channel, a 16 bit DMA channel and the associated command and control lines. LED targets are controlled via a serial I/O channel. If Camera Status is only a monitoring function, status data can be appended to the 10 bit video data. If command of the camera housekeeping proves necessary, another I/O channel will be needed; one channel for two cameras.

The computer programs fall into three categories: 1) target acquisition, 2) target tracking, and 3) system calibration. Single camera examples of the first two types of software were created during the course of this study and elements of all three types were used for the experiments and demonstration portions of this study.

The flow chart in Figure 5 and the following sections explain the essential features of the system software. The main measurement program is TBOSS. TBOSS handles the operator dialog and the transitions between acquisition and tracking. Calibration is done another program using many portions of TBOSS.

### 2.2.1 Target Acquisition

The system software begins target acquisition by a call to the subroutine ACQUIR. This subroutine turns on all the LEDs and causes camera 1 to begin a raster scan of the field of view. Subroutine SEARCH moves camera 1 scan in x and y increments equal to one-half the image dissector aperture size. At each position in the field of view, the camera measures the scene flux and returns a numerical value to SEARCH. SEARCH calculates the difference between the signal and the neighboring background. If the signal exceeds the background by predetermined threshold value a target is found. The magnitude of the threshold value is based upon background level and signal-to-noise ratio needs of the system. (See Section 3.2.5 for a further discussion.)

Once a target signal is found, TGTVAL is called upon to validate the signal. TGTVAL checks the target list to determine if current camera 1 scan coordinates represent a new target or a repeat of an earlier discovered target. If no target is listed at or near the current coordinate, the signal-to-noise ratio above background is measured. If the

---

\*Appendix contains a paper describing the operating principles of image dissector tubes and cameras in tracker applications. The main text of this report assumes the reader has a basic understanding of this device.

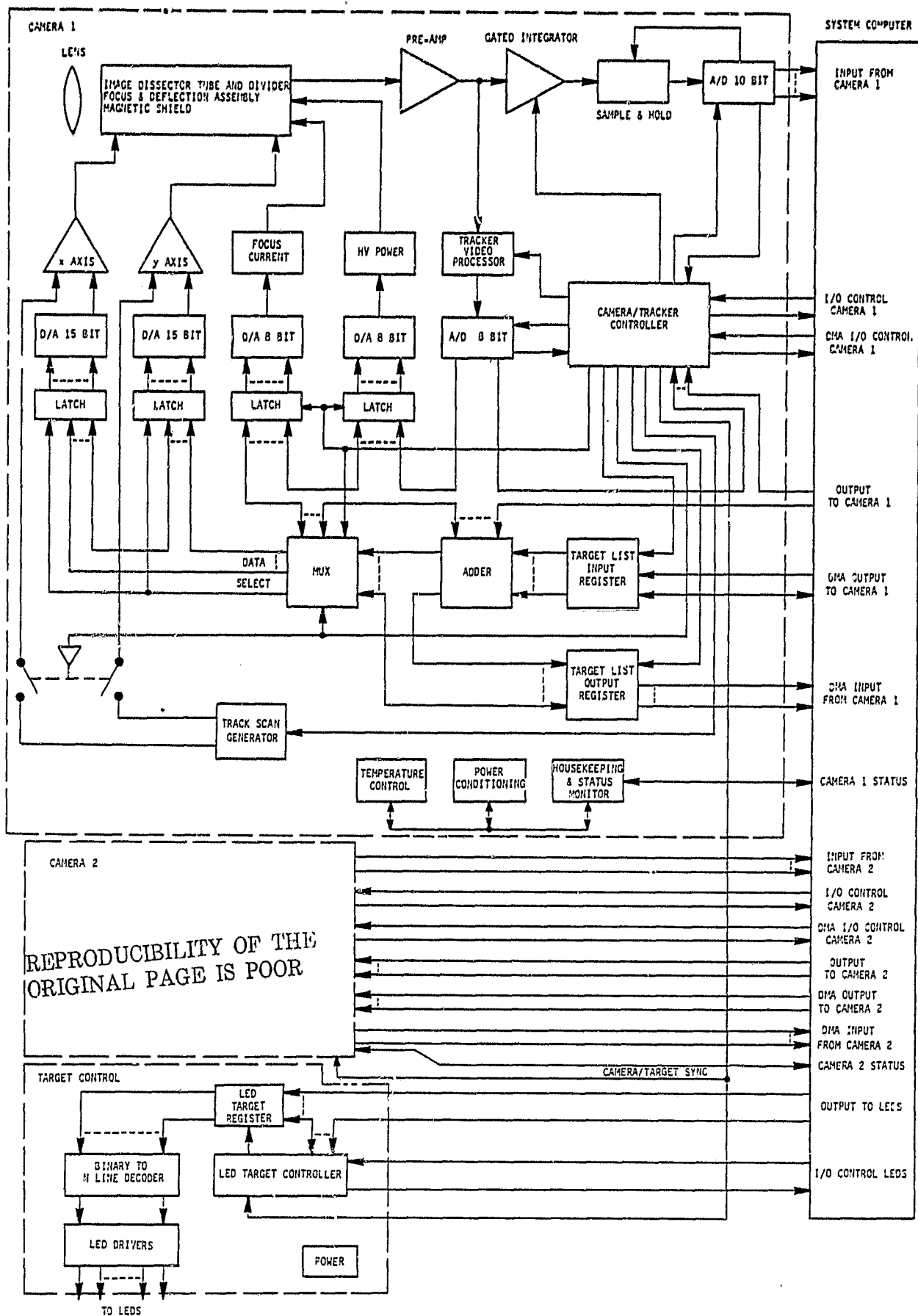


Figure 4. System Electrical Block Diagram

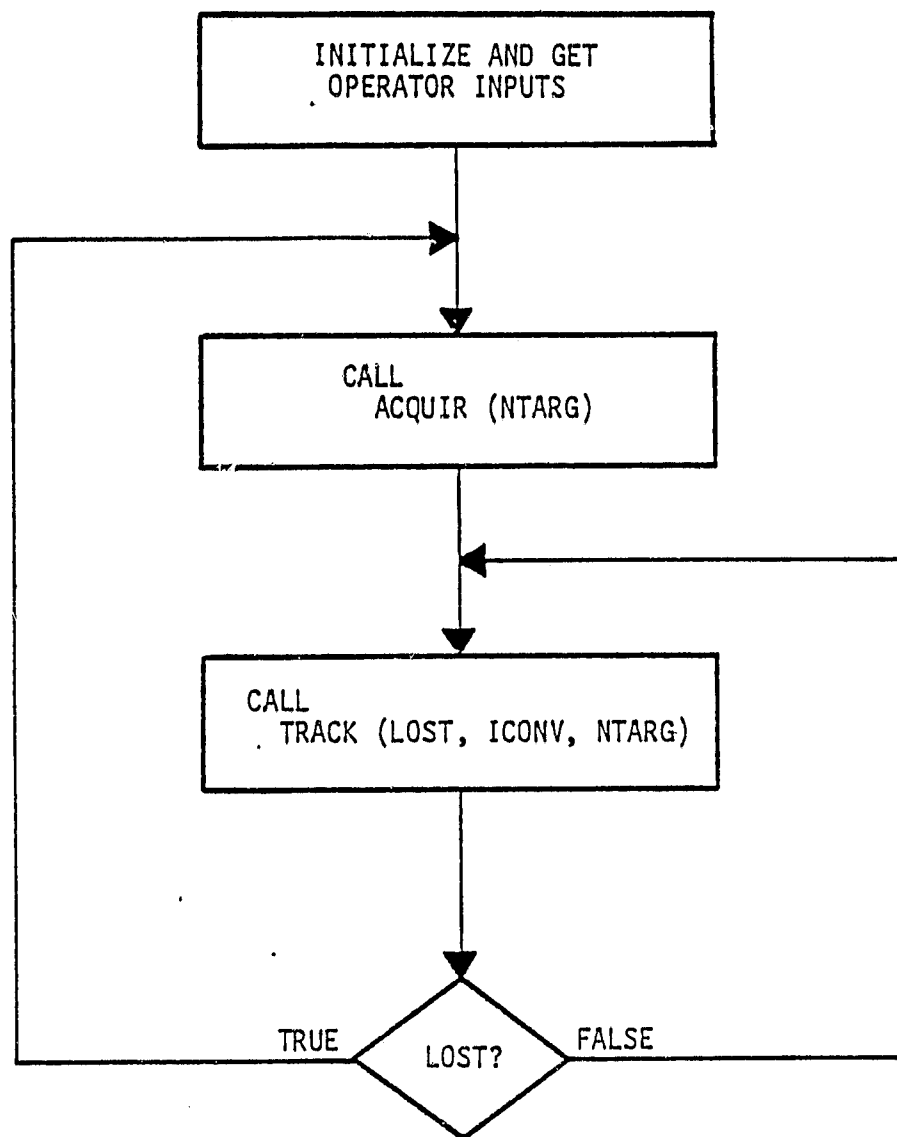


Figure 5. Program TBOSS Flow Chart (Sheet 1 of 3)



REPRODUCIBILITY OF THE  
ORIGINAL PAGE IS POOR

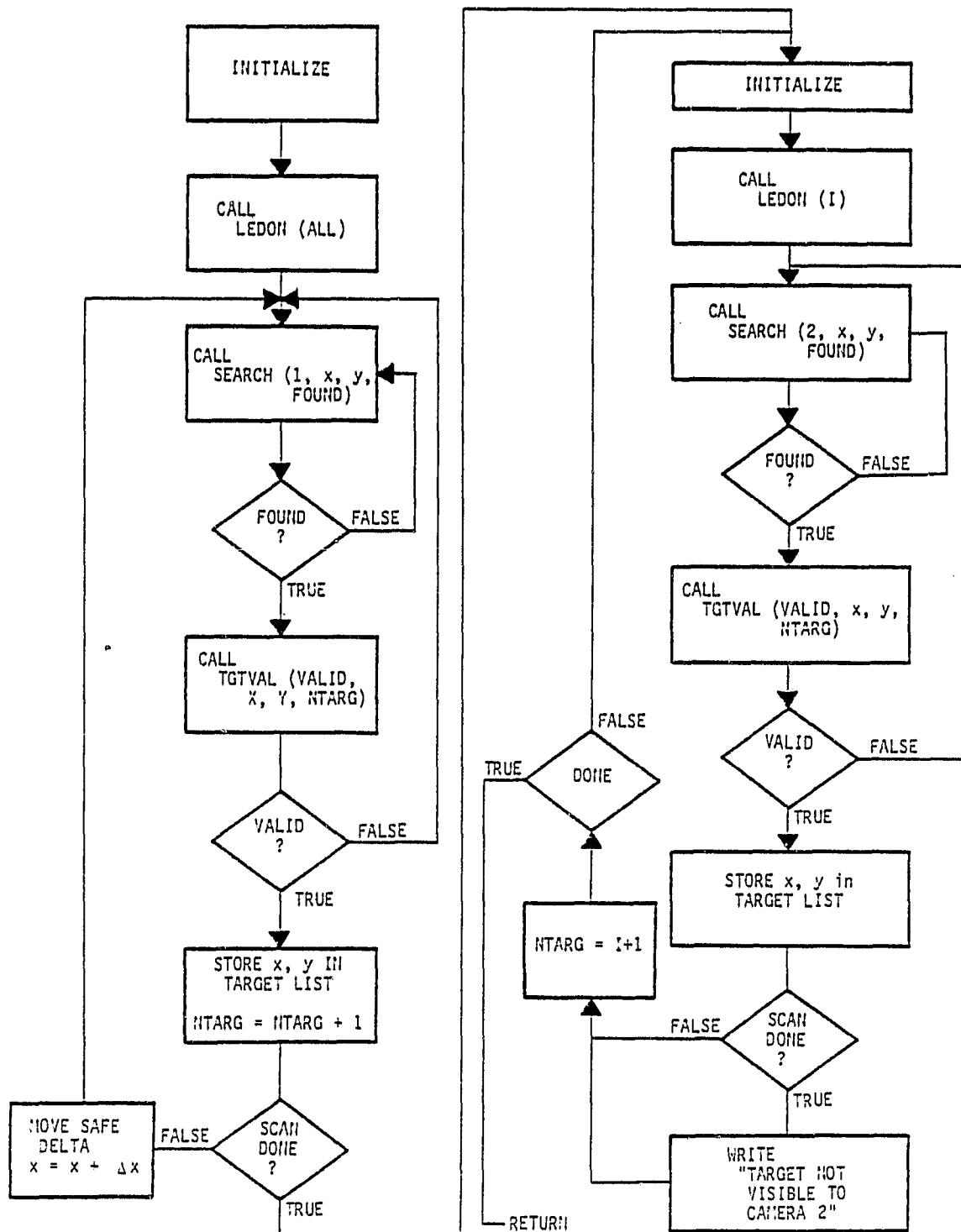


Figure 5. Program TOBSS Flow Chart (Sheet 2 of 3, Subroutine ACQUIR)

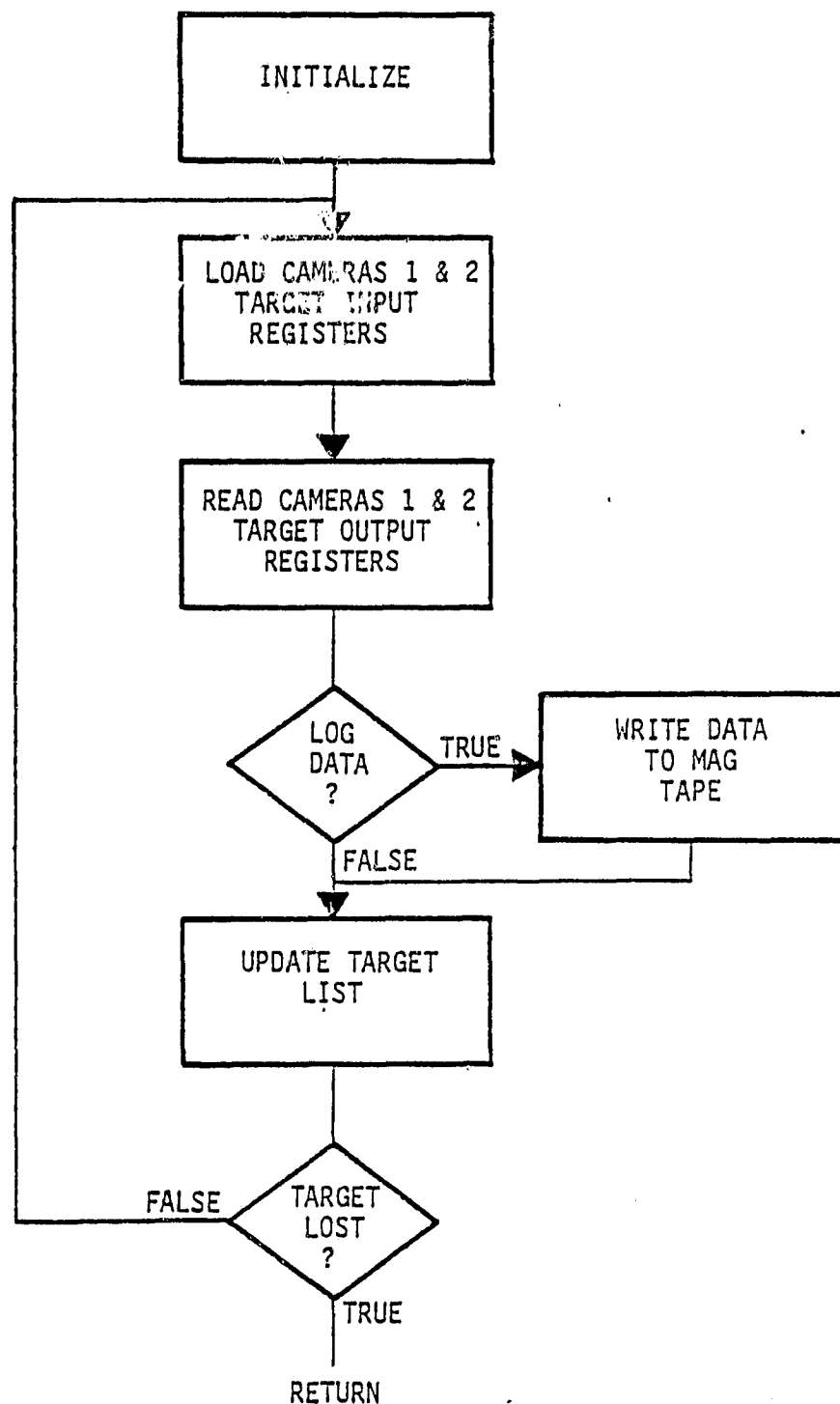


Figure 5. Program TBOSS Flow Chart (Sheet 3 of 3, Subroutine TRACK)

signal-to-noise ratio meets the system needs, the current coordinates are added to the target list. If a target already exists at or near the current coordinate, or if the signal-to-noise is less than the minimum required, the target list is not changed and the acquisition scan is resumed. Acquisition scan continues until the next above threshold signal or until the entire field of view is scanned.

The time,  $T$ , required to do a search is a function of the size of the field of view, the image dissector aperture, and the number of targets

$$T = \frac{K_1^2 S^2 t_1^2}{d^2} + N t_2$$

where

$K_1$  is a constant relating the scan step size to the image dissector aperture size; typically  $1 < K_1 < 4$ .

$S$  is the size of the field of view at the camera faceplate;

$S = 10 \times 10$  mm. (See Section 3.1.)

$d$  is the size of the image dissector aperture;  $d = 200 \times 200$   $\mu$ m. (See Section 3.4.)

$t_1$  is the time to access, measure and test the brightness value against threshold;  $t_1 \approx 10^{-3}$  sec.

$N$  is the number of targets

$t_2$  is the time to measure the signal-to-noise ratio and update the target list,  $t_2 = 0.2$  sec.

$$\begin{aligned} T &= \frac{(2^2)(10^2)(10^{-3})}{(0.2^2)} + 50(0.2) \\ &= 10 + 10 \text{ seconds} \end{aligned}$$

for 50 targets.

Each camera can go through the acquisition sequence independent of the other camera; creating its own target list. The two target lists must, however, be reconciled. Both cameras, when measuring target positions must view the same target at the same time. Failure to measure moving or vibrating targets at the same time at each camera site leads to erroneous three dimensional position results. The target is at two different three dimensional positions, neither of which has full stereographic data.

Two, reconciled target lists are obtained by causing camera 1 to scan the field in acquisition as described and shown in the Figure 5 flow chart. Before camera 2 begins its scan, all target LEDs but the

ith on the camera 1 target list are turned off. Camera 2, via SEARCH and TGTVAL scans the field of view until the target is found or until the scan is complete. If no target is found, a message is printed. If a target is found it is positively known that target i, camera 1 corresponds to target j, camera 2. This procedure is repeated until all entries in camera 1 target list have corresponding entries in the camera 2 target list.

The average time to locate the illuminated target with camera 2, knowing only that it is from the camera 1 list, that it is the only one on and all targets are uniformly distributed over the field of view, is

$$\begin{aligned} T^1 &= \frac{1}{2} \frac{K^2 S^2 t_1^2}{d} + t_2 \\ &= \frac{1}{2} \frac{(2^2)(10^2)(10^{-3})}{(0.2^2)} + 0.2 \\ &= 5.2 \text{ seconds.} \end{aligned}$$

The time for fifty targets is 260 seconds.

Knowing where to begin the camera 2 scan, at the top or bottom of its field of view will reduce this time by almost one-half.

#### 2.2.2 Target Tracking

Following target acquisition, the system switches to the tracking mode for measurement of target positions. The computer sends the current target coordinates from the target list to each of the cameras. The tracker circuitry in each camera does the position measurement independently. Figure 6 shows the sequence of steps involved. In Figure 6, the target image shown as circular area, represents the optical point spread function seen in cross section. The image dissector aperture is square. Typical sizes are 35  $\mu$ m full width half maximum for the target image and 200 x 200  $\mu$ m for the aperture. Sections 3.1 and 3.3 provide reasons for these sizes.

The tracker scan generator causes the image dissector camera to execute a rapid, four position track scan about the estimated target position. The scan amplitude in each of the two camera scan axes is typically one-half the aperture size. (See Section 3.5.) The seven step sequence positions the center of the scan pattern to the center of the target.\* The center of the scan pattern is eventually returned to the computer to update the target list of each camera and to be recorded as the target position. This sequence is repeated over and over for each target.

---

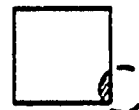
\*Actually, the scan goes to a position having equal integrated brightness at each of the four sample positions.

$(X_o, Y_o)$  IS THE ESTIMATED TARGET CENTER

1. GO TO  $(X_o + \Delta X, Y_o)$   
MEASURE BRIGHTNESS



2. GO TO  $(X_o - \Delta X, Y_o)$   
MEASURE BRIGHTNESS



3. CORRECT  $X_o$   
$$X_o = X_o + G_x \left[ \frac{B1 - B2}{B1 + B2} \right]$$



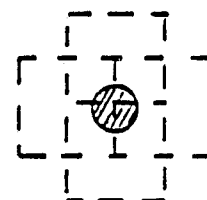
4. GO TO  $(X_o, Y + \Delta Y)$   
MEASURE BRIGHTNESS



5. GO TO  $(X_o, Y - \Delta Y)$   
MEASURE BRIGHTNESS



6. CORRECT  $Y_o$   
$$Y_o = Y_o + G_y \left[ \frac{B2 - B4}{B3 + B4} \right]$$



7. GO TO STEP 1.

$G_x$  AND  $G_y$  ARE CONTROL LOOP GAINS.

Figure 6. Point Tracker Operating Principle. The X and Y Co-Ordinates are with Respect to the Scan Axes at the Camera

There are several properties that describe the position measurement and tracking process. The first property is capture range.

- 1 Capture range is a vector measure of how far the target center can be from the center of the track scan and still permit the track scan to converge upon the target center position. Capture range is measured perpendicular to the camera line of sight. In first approximation, the capture range falls within the area covered by the convolution of the track scan with the target image. For the example described here, the capture range is shown in Figure 7.\* For successful operation, the target position estimate, after acquisition or when periodically returning to the target, must fall within the bounds of Figure 7. The size of the capture range sets a limit on the amplitude of the target vibrational motion.\*\* For the Figure 7 case, the limit is approximately  $\pm 235 \times \sqrt{2}/2 \mu\text{m}$  or  $\pm 165 \mu\text{m}$  ( $\pm 21 \text{ mm}$  at the model). In some special cases, vibrations parallel to the camera scan axes, the limit is as large as  $\pm 220 \mu\text{m}$  ( $27 \text{ mm}$  at the model).
- 2 A second descriptive property is the number of track scan cycles used to converge to the target center position. The number of cycles to converge is a function of the offset distance between target and the track scan. Experiment results of Section 3.5 show, for targets at the extreme of the capture range, 8 to 12 track scan cycles are needed. For target offsets less than  $50 \mu\text{m}$ , one-fourth the aperture size, the convergence is completed in four or fewer cycles.
- 3 The third property is termed convergence criterion. Convergence criterion is the maximum acceptable uncertainty in the location of the target center. In the limit, for an image dissector tracker, the uncertainty in target position depends mainly upon the signal-to-noise ratio of the illumination falling on the photocathode. In practice other terms such as the deflection axis D/A converter resolution, target or camera vibration, seeing conditions through the boundary and shock layers also enter. The experiments in Section 3.5 show that  $\pm 0.5 \mu\text{m}$  is possible at the photocathode for electrical signal-to-noise ratios of 30:1 RMS. Vibration effects and seeing conditions are assessed in Section 3.6.

---

\* The capture range at the model depends upon the range to the model, the view angle, the attack angle and the position in the field of view. The size at the model can be estimated for zero angle of attack at the center of the field of view and  $1650 \text{ mm}$  range by multiplying the Figure 7 dimensions by 125.

\*\*Section 3.3 shows target loss is expected to be infrequent. The system is programmed to skip to the next target on the list upon loss of signal. The dropout target is re-examined the next time through the target list. If all targets are lost the system switches to acquisition.

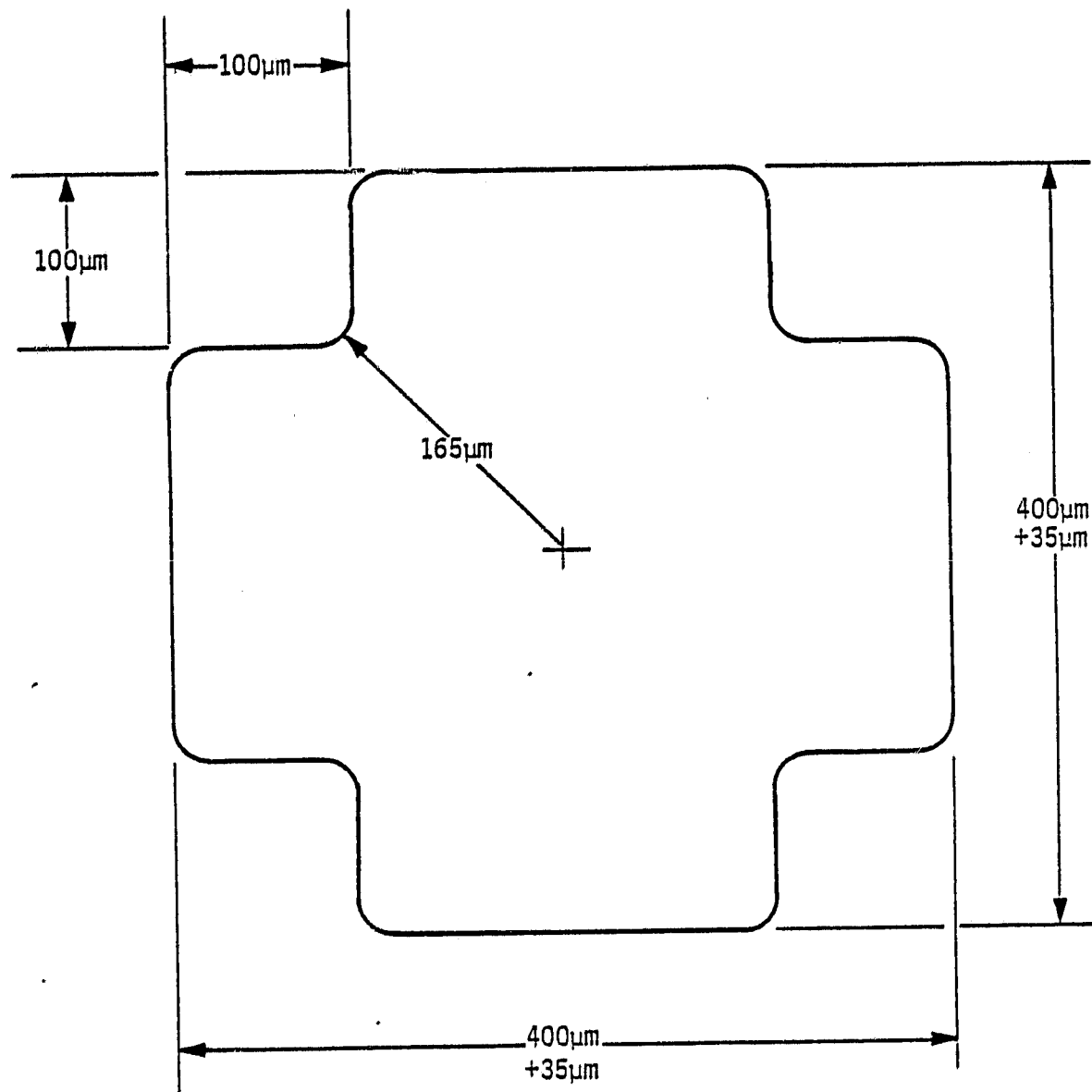


Figure 7. Capture Range for a  $200 \times 200 \mu\text{m}$  Image Dissector Aperture and a  $35\mu\text{m}$  Point Spread Function

- 4 A fourth property used to describe the measurement and tracking process is the time required to do one cycle or more of the Figure 6 sequence. The tracker hardware is specifically designed to execute the tracking scan and signal processing algorithm. It causes the camera to scan the target, it processes the video, corrects the scan position, and returns the corrected value to the computer.

Figure 8 is a timing diagram of the tracker action for one of the two cameras. The camera goes to the +X scan position and integrates the signal for 20  $\mu$ s. The time to store the +X value and go to the -X scan position is 5  $\mu$ s. The video at -X is then integrated for 20  $\mu$ s. The next 40  $\mu$ s are used to update the estimate of the target X axis position and to send the camera to the +Y scan position. The signal integration sequence for + and -Y positions is the same as for the X position. Again, 40  $\mu$ s are needed to update the estimate of the target X position and to send the camera back to the +X scan position. If the camera goes to the next target, 70  $\mu$ s are needed to update the estimate of the current target Y position, store X, Y and send the camera to the estimated position of the new target.

The time to do 1 cycle is  $t_1 = 130 \mu$ s.

The time to do n cycles on one target is

$$t(n) = (n) 130 \mu\text{s} + (n-1) 40 \mu\text{s}.$$

The time to do N targets of n cycles each is

$$\begin{aligned} T(N,n) &= Nt(n) + (N-1) 70 \mu\text{s} \\ &= Nn 130 \mu\text{s} + N(n-1) 40 \mu\text{s} + (N-1) 70 \mu\text{s} \end{aligned}$$

For example if  $N = 50$  targets, and

$$n = 3 \text{ cycles per target}$$

then  $t(1) = 130 \mu$ s

$$t(8) = 470 \mu\text{s}$$

$$T(50,3) = 27 \text{ ms}$$

This is a rate of 1800 targets per second. The highest rate would be for  $n = 1$  or 5000 targets per second.

Not all targets can be measured to an uncertainty within the convergence criterion in a single cycle. Neither do all targets require 3, 8, or even 12 cycles. It is advantageous to make the tracker adaptive. The tracker remains at a target until the convergence criterion is met or until a maximum number of track scan cycles have been completed; then goes to next target.\*

---

\*This action was included in the demonstration software.



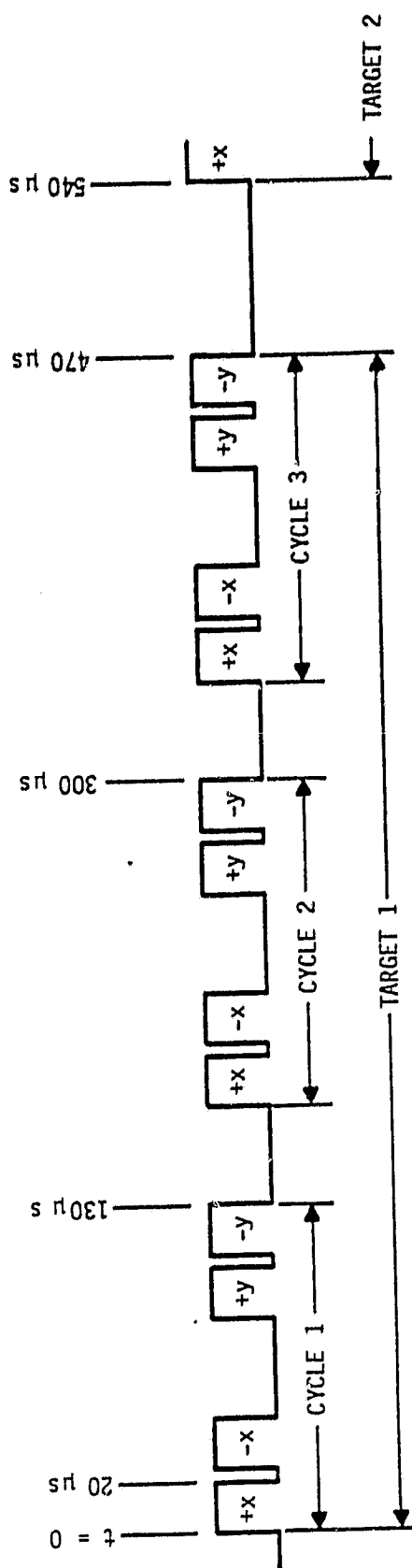


Figure 8. Tracker Function Timing Diagram

2.2.3 System Calibration - The system user needs to know the transformation function between model space coordinates and tracker system output data. More specifically the user needs to know how the system differs from the mathematical model built into the data analysis software.

The transformation program currently being used at NASA Langley for photogrammetry corrects for symmetric and anti-symmetric lens and camera distortion in a manner similar to the one used to determine viewing angles and camera distances. That is, it is a least squares coefficient fitting technique using known position of reference points. It is thought that some reduction in computational effort could be achieved by measuring the mapping function of the camera, lens, pressure vessel window and perhaps even a test section window in calibration fixture outside the tunnel. Section 3.6.1 describes an interpolating distortion correction method that is estimated to provide correction to  $\pm 0.5 \mu\text{m}$  at the camera photocathode. The camera, lens and windows with a correction algorithm and data base would then yield a system having a linear mapping function  $\pm 0.5 \mu\text{m}$  X magnification between the object plane and camera data output.

The data base is obtained by mapping the field of view of each of the two cameras. It is assumed the distortion is a slowly changing function of target position within the field of view and that a finite number of points are sufficient to describe the function. (Section 3.6.1 shows that 625 points are needed.)

The test fixture must have means to move a point source of light about the field of view. Such a means is an array of LEDs located at known positions on a flat plate. There must be provisions to assure the plate is 1650 mm from the camera and that it is perpendicular to the optical axis. Variations on the acquisition and tracking software gather the distortion map data. An analysis program is used to create the calibration data base.

The camera and lens distortion calibration map is either provided with the recorded tunnel test data or could be used to correct the recorded data before the data is given to the experimenter. Since the tracker system must operate in real time when recording data, it is better to do distortion corrections off line, after all data is collected.

Estimates of the optical window and the optical path seeing conditions upon the measurement accuracy are given in Section 3.6.

It is still necessary to calibrate mm at the model as a numerical value in the software. The stereographic method being considered here is a non-metric method in the projective geometry sense. This means that sizes or scale factors are not preserved and thus must be calibrated. It also means that the exact viewing angles of both cameras and their separation distance need not be known. The method<sup>1</sup> does need at least 6 and preferably as many as 20 reference points surrounding and throughout the volume of the combined two camera field of view. The reference points must not be in the same plane.

<sup>1</sup>Top cit page 1

This portion of the calibration must be done in the tunnel with camera installed. The 0.6 to 20 reference points can be specific targets of known location on the model. This calibration should be done at test temperature and pressure as part of the data logging process.

### 2.3 System Computer

The computer used in this system must be capable of supporting the operation of the two image dissector cameras, the target LEDs, a magnetic tape recorder, a CRT operator terminal, and printer. It may also be desirable to have a card reader and a floppy disc unit for ease of programming and program modifications.

During acquisition mode, each of the two image dissector cameras are controlled via 16 bit, duplex interfaces. Instruction words are used to set internal camera conditions and to select or not to select the tracker mode. LEDs operate via serial interface. Instructions are sent only when a change in operation is required.

Two words are required for each (X,Y) coordinate. If one coordinate is unchanged, only the one word is needed. The rate during acquisition is 1000 coordinates per second, set mainly by software execution time.

Scene flux measured at selected coordinates is returned to the computer as single 16 bit words. The rate is again 1000 measurements per second.

During track and measurement mode, the exchange between computer, LEDs and the two cameras occurs at a 40 K word rate. The computer must, at the same time, service the magnetic tape drive at an average 20 K word rate, monitor the "log data" command from the outside, update the target list, and coordinate the actions of two cameras. The magnetic tape unit operates via a direct memory access interface. The tracker circuitry has coordinate storage buffers containing the target list. These buffers communicate with the computer via direct memory access. Thus the CPU should have ample time to observe and direct the system activities without being burdened with all the data transfers.

During calibration, the computer communicates with the cameras as already described. The target light sources are now those on the calibration fixtures.

The acquisition software is written in a high level language such as Fortran. The driver modules for the cameras and light sources are written in assembly code. The track subroutine is in Fortran. The track scan and video processing algorithm (Figure 6 sequence) is in hardware at each camera.

No estimate has been made of memory requirements. The experiments and demonstration were conducted under a real time operating system and Fortran on a computer having 24K words of memory. The main tracking program plus operating system used 16K words. For the experiments, the track scan and video processing algorithm was in Fortran.

### 3.0 ANALYSIS AND EXPERIMENTS

The design of a stereo electro optical tracker system used to measure aeroelastic deformations of wind tunnel models must consider the following essential elements.

1. The characteristics of the targets attached to the model.
2. The illumination of the targets and the model.
3. The optical properties of the media between the model and the electronic cameras.
4. The characteristics of the electronic cameras.
5. The effects of the tunnel environment and system installation upon operation.

#### 3.1 Optics

The field of view is 800 x 1000mm at 1650mm camera to model distance and zero degree angle of attack. Image dissector camera tubes are available in three sizes having photocathodes of 17, 25, and 44mm diameter. Figure 9 shows these photocathodes, the image format size, and appropriate focal length lens.

The model can be moved +/- 450mm about the nominal 1650mm distance. It is necessary to maintain focus over this range of distances. Operation off focus increases the radius of the point spread function of the lens at the image plane. The change in radius due to off focus operation can be estimated by

$$r = \frac{\Delta D_i}{2} \tan(\alpha)$$

where

$$\alpha = \sin^{-1}(1/2f)$$

f = the f number of the lens.

Large f numbers provide good depth of focus but are very inefficient collectors of light. A compromise must be achieved between depth of focus and lens aperture.

The magnitude of  $\Delta D_i$ , the change in back focal plane position, depends upon the focal length of the lens.

$$\Delta D_i \approx \left[ \frac{1}{D_o(1)} - \frac{1}{D_o(2)} \right] (FL)^2$$

for  $FL/D_o \ll 1$

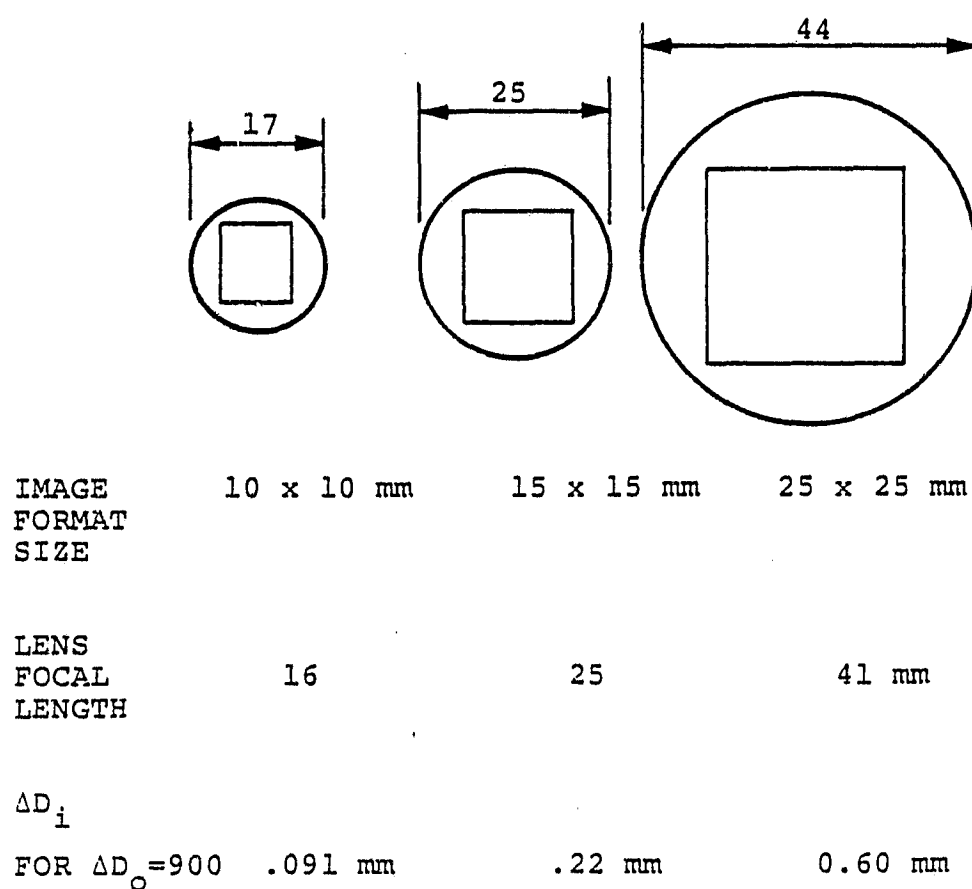


Figure 9. Camera Image Formats and Lens Focal Lengths for Three Sizes of Image Dissectors.  $\Delta D_i$  is the change in back focal plane position caused by  $\pm 450$  mm change in object position for an object at 1650 mm.

Calculated values for  $D_i$  are included in the table in Figure 8.

If  $\Delta r$  is scaled to the size of the field of view, that is

		FOV		
		10x10	15x15	25x25 mm
$\Delta r$	$\Delta r_0$		$1.5\Delta r_0$	$2.5\Delta r_0$
and FL	16 mm	25 mm	41 mm	
then the required f# is	2.8	4.5	7.3	

The results favor the use of a small format tube and short focal length lens.

The light collection efficiency of an f/7.3 lens is only 15 percent of the collection efficiency of the f/2.8. It is shown in Section 3.2 that such a loss is not desirable.

The growth in the point spread radius for the f/2.8, 16mm lens is  $r = \frac{.091}{2} \tan(10.3) = 8\mu\text{m}$ . This value is tolerable. The electron optics of the image dissector camera tube exhibit a 5-10 $\mu\text{m}$  radius point spread. An f/2.8 lens has a finite point spread radius also, about 1 $\mu\text{m}$  theoretically but more likely 5-10  $\mu\text{m}$  in commercially available unit of conventional design. Thus the 8  $\mu\text{m}$  change in point spread radius should be compared to the 10-20 $\mu\text{m}$  radius point spread. It is shown in Section 3.5 that absolute size of the point spread is of lessor importance than changes in size.

The important properties of the tracker lens are low distortion, 0.5%, flat focal plane,  $\pm 10 \mu\text{m}$  symmetrical aberrations, low scattered light, and mechanical stability.

### 3.2 Targets

Targets cannot be considered without also considering some aspects of target illumination and tracking method. The model can move in pitch, roll and yaw over a substantial fraction of the tracker system field of view. Thus the target appearance can change substantially. The ideal solution is a combination of targets, illumination, and tracking method which yields a position measurement accuracy independent of changes in

1. Target size - magnification
2. Target orientation - rotation
3. Target shape - distortion
4. Target illumination - magnitude, uniformity
5. Target contrast - stray light
6. Target focus - depth of focus
7. Target viewing angle - off normal view

The target and its illumination must also be optically efficient in terms of power input to the illuminator for the signal needed at the camera.

3.2.1 Point versus finite sized targets. - There are two general classes of targets; point and finite. Point targets are not resolved as a disc image by the camera and optics. Finite targets have a definable size, shape and even structure.

Point targets can be defined quantitatively as having an image whose size is less than one-third the size of the camera optical spread function. The section on camera optics estimated the radius of the spread function to be  $10\text{--}20\text{ }\mu\text{m}$  plus a 0 to  $8\text{ }\mu\text{m}$  term for depth of focus effects. Using the dimensions of Figure 1 and a 16mm FL lens, the smallest demagnification is about 75 at a range of 1200mm. The size of the target, at the model, is therefore  $2 \times 750\text{ }\mu\text{m}/3 = 500\text{ }\mu\text{m}$  or less diameter.

Target position for point targets is measured by making four samples in the vicinity of the target image as shown in Figure 6. The position of the four samples is adjusted until all have equal signal amplitude.

Numerous types of finite targets can be considered. In general finite targets require more image samples than point targets because of the range of sizes and possible orientations.

Two simple examples of finite targets are the white circle in a black surround or the black and white wedge.

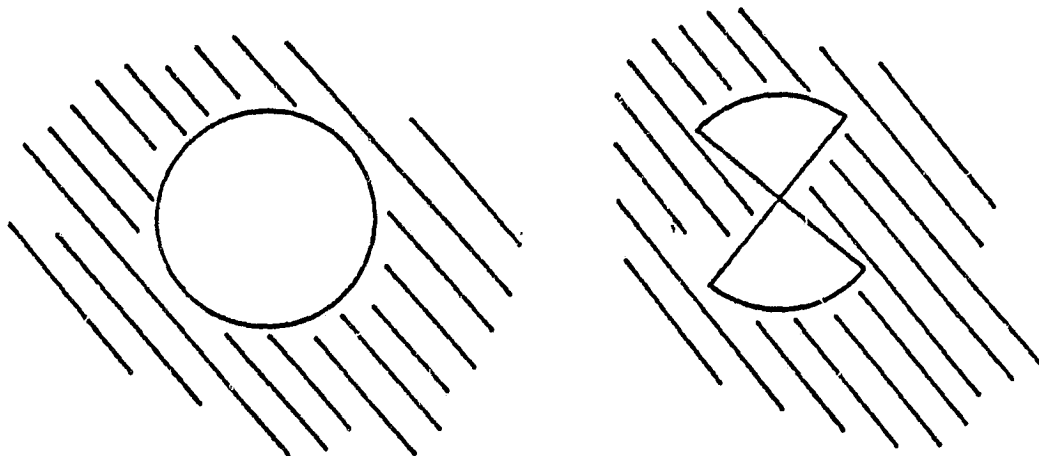


Figure 10. Two Examples of Finite Targets

Since the model can move in range and pitch angle, these targets in the extreme can look like those shown in Figure 11. A scanning method which is independent of these size and shape changes is a raster whose dimensions are greater than the maximum possible target size. The scanned data is then used to compute the center of brightness; assuming a uniform target. This method is time consuming if done by computer or complicated electronically if done by a dedicated hardware processor.

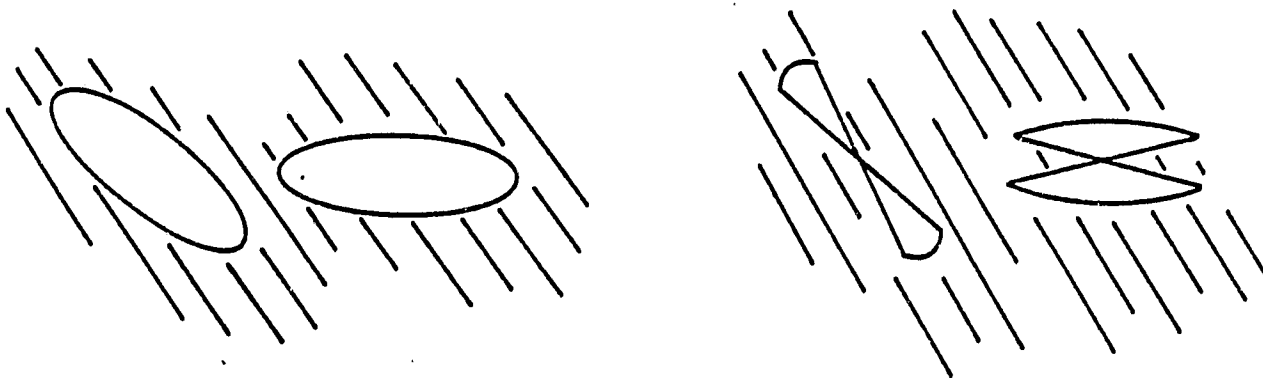


Figure 11. Finite Targets Viewed at Large Angles

A less complex or time consuming method uses a circular scan pattern. The method seeks the black white edge crossings and adjusts the center of the scan circle until two pairs of edge crossings are each  $180^\circ$  apart. This method is sensitive to target rotation. The rotation must be known or measured before proper adjustment of the scan center occurs.

In general, finite targets require a tracking and measurement method insensitive to size and shape changes. Finite targets are best used where some useful information is conveyed by their size, shape, or pattern.

3.2.2 Active versus passive targets. - Targets can be either active sources of light or passive reflectors of light. Active point targets such as light emitting diodes are optically very energy efficient. All the energy contributes to the source intensity. Fiber optic light pipes are a bit less efficient due to losses along the fibers and at the input coupling. Nonetheless, optical fibers viewed end on are potentially good targets.

Passive point targets such as diffuse painted patterns, are optically very inefficient in this installation. Only a small fraction of the incident energy is reflected to the cameras. Passive point targets can be illuminated by a spot light that moves in step with the tracker as the tracker moves from target to target. Such a scheme would require either premapping of all nominal target positions versus angle of attack, or, real time computation of illuminator pointing angles. It is still necessary to illuminate an area larger than the passive target since an allowance for pointing errors must be made.

The flux onto a target, at normal incidence is given by

$$F = B_o A \frac{4\pi f^2 \text{SNR}^2 M^2 K \epsilon_1 \epsilon_2}{S \Delta t}$$



where

- $A = 1 \times 10^{-6} \text{ m}^2$ , the area of a point target
- $f = 2.8$ , the focal ratio of the lens
- $\text{SNR} = 30$ , the signal-to-noise ratio needed according to Section 3.5.2
- $M = 125$ , the demagnification between target and image
- $K = 2.3$ , the noise factor of the camera
- $e = 1.602 \times 10^{-19}$  coulombs/electron
- $\epsilon_1 \epsilon_2 = 1$ , reflection and lens transmission factors
- $S = 200 \text{ } \mu\text{A/lumen}$ , the camera sensitivity
- $\Delta t = 20 \text{ } \mu\text{s}$ , the time to make one brightness sample

$$F = B_0 A = \frac{4\pi(2.8)^2(30)^2(125)^2(2.3)(1.6 \times 10^{-19})(1)(1)}{(200 \times 10^{-6})(20 \times 10^{-6})}$$

$$= 0.13 \text{ lumen}$$

The target is only  $1 \times 10^{-6} \text{ m}^2$  in area, yet the flux is 0.13 lumens. The illuminance must therefore be  $1.3 \times 10^5 \text{ lumen/m}^2$ . This is direct sunlight. For flood illumination of the  $1\text{m}^2$  field of view at the model, this is at least 8 Kw of quartz-iodide lamps in housings with very efficient reflectors. For a moving spot of illumination using a  $10 \text{ cm}^2$  area this is about 250 watt of quartz-iodide illumination with an  $f/2$  projector lens.

A corner cube reflector used as a passive point target can be energy efficient. A collimated beam of light to a corner cube is reflected back along the same path to the source. A corner cube target does not exhibit the depth of focus effects previously mentioned because the source appears to be located at infinity. There are two major problems with corner cubes; size and view angle. It is not clear if millimeter sized cubes are available at an economical cost. Corner cubes do not work at large angles ( $45^\circ$ ) of incidence.

In general, active, point targets such as LEDs are preferred.

3.2.3 Target contrast. - Contrast between target and surrounding model is an important property. A point target tracker can, in principle, operate on low contrast targets. In practice, the background signal should be eliminated to minimize the dynamic range of the electronics and to remove the effects of background flux changes.

Let  $F_0$ ,  $F_1$ , and  $F_2$  be the average values for the background, sample 1, and sample 2 signals for the Figure 6 tracking method. Associated with each sample is a noise  $n_0$ ,  $n_1$ , and  $n_2$ , each proportional to the square root of their respective signals. The track scan position error signal,  $E$ , is:

$$\epsilon = C_1 \frac{(F_1 + F_0) - (F_2 + F_0)}{(F_1 + F_0) + (F_2 + F_0)} = C_1 \frac{F_1 - F_2}{F_1 + F_2 + 2F_0}$$

It is possible to remove the  $2F_0$  term by making a measurement of the background signal. This additional measurement will add 20 to 60  $\mu$ s to the single cycle time shown in Figure 8.

Removal of the  $2F_0$  term does not completely solve the background problem. At null position,  $F_1 = F_2$ , the finite noise associated with each of the samples becomes important. The noise,  $e$ , about the null position is equal to

$$e = C_1 \frac{(2n_0^2 + n_1^2 + n_2^2)^{1/2}}{F_1 + F_2 + (2n_0^2 + n_1^2 + n_2^2)^{1/2}}$$

If  $F_0 = F_1$ , 50 percent contrast, then the position noise about null is at least  $\sqrt{2}$  times greater than with zero background. As  $F_0$  becomes larger than  $F_1$ , a still lower contrast, then  $n_0$ , the noise in the background signal becomes the dominant\* term.

If  $F_0 \leq 0.1 F_1$ , a condition corresponding to >90 percent contrast, background measurement and subtraction is not necessary. If  $F_0 = 0.1 F_1$ , the noise about null is only 5 percent greater than the zero background case; an acceptable condition.

Tracker control loop gain depends upon the  $2F_0$  term in the error signal equation. For  $0 \leq F_0 \leq 0.1 F_1$ , the change in loop gain is less than 1 dB, an acceptable value. (See Section 3.5.)

The limits on absolute background brightness and the needed target intensity can be estimated for a system using LED targets. Section 3.5 shows that the required signal-to-noise ratio for the difference between target and background is 30:1 RMS. This signal-to-noise ratio allows the center of the target to be located at  $\pm 0.5 \mu$ m at the model for zero angle of attack and center of the field of view.

---

\*Image dissectors will respond to the 120 Hz ac flicker from incandescent or fluorescent lights. This can increase the  $b_0$  noise term considerably beyond the shot noise value.

Let  $I_0$  and  $I_1$  be the photocurrents entering the aperture of the image dissector due to the background and the target plus background. It is required that the signal-to-noise ratio of  $I_1 - I_0$  be greater than or equal to 30. Since the image dissector is a shot noise limited device, the noise in each of the two photo currents is

$$i_0 = \left[ \frac{ekI_0}{\Delta t} \right]^{1/2} \quad \text{amperes}$$

$$i_1 = \left[ \frac{ekI_1}{\Delta t} \right]^{1/2} \quad \text{amperes}$$

where

$$e = 1.602 \times 10^{-19} \text{ Coulombs/electron}$$

$$k = 2.5, \text{ image dissector noise factor}$$

$$\Delta t = \text{sample time, } 20 \text{ } \mu\text{s in this system.}$$

$$\text{SNR} = \frac{I_1 - I_0}{(i_0^2 + i_1^2)^{1/2}} = \frac{I_1 - I_0}{\frac{ek}{\Delta t}^{1/2} (I_1 + I_0)^{1/2}}$$

These equations assume no ac modulation of the background. If there is ac modulation,  $i_0$  becomes the rms value of the modulation. As calculated here the equation gives the greatest dc  $I_0$  value that is tolerable. The noises are assumed to be uncorrelated and to add in quadrature.

Figure 12 is a plot of  $I_1 - I_0$ , the required target photo current versus background photo current  $I_0$  for  $\text{SNR} = 30$  and  $\Delta t = 20 \text{ } \mu\text{s}$ . An additional abscissa scale on the plot shows the maximum background luminance at the model for 2854°K tungsten illumination, f/2.8 lens and a 200 x 200  $\mu\text{m}$  aperture in the image dissector. General office illumination is of the order of 100 lumen  $\text{m}^{-2}$  steradian $^{-1}$ .

The extra scale on the ordinate axis gives the target source intensity to cause the signal photo current. This intensity is based upon an f/2.8 lens and a red LED. Red LEDs produce  $1 \times 10^{-4}$  watts/steradian at 60 mA, current, 25°C, and normal incidence.

Undoubtedly, there will be other sources of light used within the tunnel. These sources could be incandescent, fluorescent, or laser. They may even be turned ON and OFF for various reasons and will probably operate from the ac line. It is prudent to make the tracking system as insensitive as possible to these sources.

There are several means available to achieve this end. First, make the targets the most intense source within the tunnel. LEDs can be pulsed to intensity levels 20-100 times greater than their dc, 25°C ratings for 1 percent duty cycle at 300 Hz pulse rate. In this system, the target diode would be turned ON only when the particular target position is being measured. This will require a small amount of circuitry in the model in addition to LED controller described in Section 2.2.

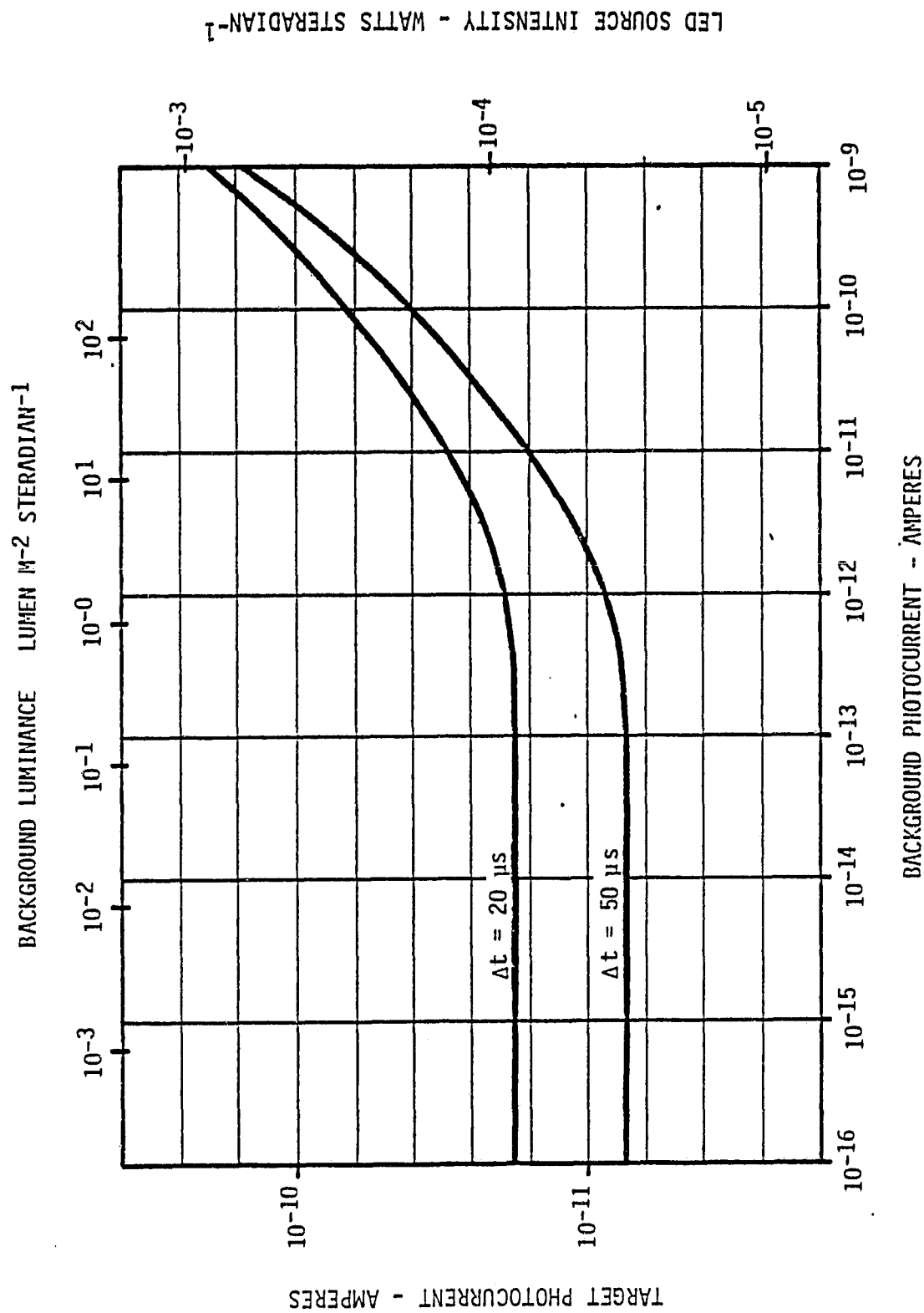


Figure 12. Target Intensity Versus Background Luminance LED Point Target  $\lambda = 655$  nm  
 Photo Cathode Sensitivity 30 mA/watt, 200  $\mu$ A/lumen  
 Lens  $f/2.8$ ,  $T = 0.8$   
 Aperture 200 x 200  $\mu$ m  
 Sample Time 20, 50  $\mu$ s  
 Signal-to-Noise Ratio 30:1 RMS, Noise Factor  $k = 2.5$

Further reduction in system susceptibility to background illumination can be obtained by using narrowband optical filters on the cameras. If a filter with a passband of 50 nm centered on the 655 nm LED emission wavelength is used, the insertion loss will be about -3 dB. The out-of-band transmission is usually less than -60 dB.

With this kind of optical filter, background light due to tungsten sources would be reduced by -13 dB, due to cool white fluorescent sources by -19 dB, but only 0 to -3 dB against HeNe laser sources.

Added discrimination against HeNe laser light can be obtained by using a narrower bandpass and accepting a greater insertion loss or using the less efficient green LEDs. The problem is the emission wavelengths of red LEDs, and particularly the high efficiency red LEDs, overlap the HeNe laser wavelength.

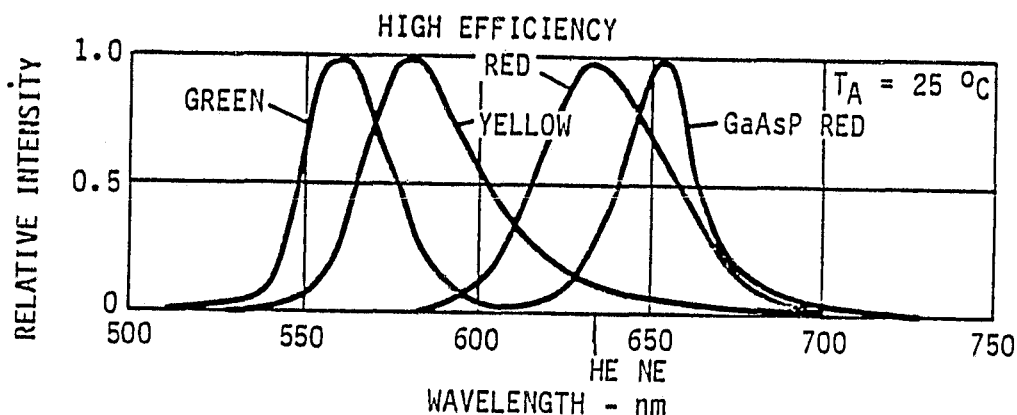


Figure 13. LED Relative Intensity Versus Wavelength

If the narrow band optical filter does not provide sufficient discrimination between target and background, a phase coherent, modulated light system could be considered. Each of the target LEDs would be modulated at a frequency in the range of 5 MHz. Since the image dissector tube will pass this frequency, a tuned amplifier, phase sensitive detector would replace the conventional preamp. The system would accept optical radiation within the optical filter passband having an amplitude modulation of 5 MHz and the proper phase relationship to a reference signal. This is a complicated approach and is an extreme but effective measure. This approach avoids the 20 to 60  $\mu$ s time penalty associated with measuring the background. The 50 percent duty cycle of the 5 MHz modulation doubles the needed target intensity.

3.2.4 Angular distribution of the target light. - An almost hemispherical distribution of light from the target is essential.

For a flat plate at zero angle of attack the cameras view targets at a  $35^\circ$  angle from normal incidence. As the flat plate changes angle of attack, the  $35^\circ$  angle sweeps over a range of angles from  $16^\circ$  to  $54^\circ$ . The camera has a rather wide field of view,  $34^\circ$ , therefore a nominal  $35^\circ$  viewing angle at the center of the field of view becomes  $18^\circ$  to  $52^\circ$  at the sides of the field of view for zero angle of attack and  $-1^\circ$  to  $71^\circ$  for  $19^\circ$  angle of attack. The greatest viewing angle is about  $72^\circ$  for  $19^\circ$  angle of attack and occurs in the corner of the field of view. If targets are mounted on curved surfaces, this can lead to still larger viewing angles.

For a target having a Lambertian distribution, the intensity varies as  $\cos\theta$ , where  $\theta$  is the viewing angle from the normal. At  $\theta = 70^\circ$  the target intensity is only one-third of the normal value. LEDs are not Lambertian. Intensity at  $70^\circ$  is about 10 to 20 percent of on axis intensity. Stated differently, the brightness required for off axis viewing will determine the target source intensity. This fact alone will likely dictate pulsed operation of the LED targets.

### 3.3 Target Dynamics

Vibrations of the model will occur during tests. The vibrations will primarily be rigid body motion of the model on the sting and bending motion of the wings. Targets attached to the model will therefore vibrate about some average position.

Table 1 gives the amplitudes and frequencies of the largest or most rapid vibrations as provided by NASA for this study. The motions at the model were transformed to motions at the camera image plane using the parameters

$X_O =$	946 mm	$\alpha =$	$125^\circ$
$Y_O =$	- 400 mm	$\beta =$	$90^\circ$
$Z_O =$	-1352 mm	$\gamma =$	$35^\circ$

and a back focal distance of 16.157 mm. These are the conditions illustrated in Figures 1 and 2.

Other motions of the targets, such as those which occur with angle of attack changes, take place much less rapidly or are of very much smaller vibrational amplitude.

All the motions given in Table 1 are excursions about an average position. The largest distance is  $2 \times 63 \mu\text{m} = 125 \mu\text{m}$  peak-to-peak at the camera for the 8-50 Hz yaw motion. The capture range of the tracking system should be larger than this dimension to avoid the need to periodically reacquire a lost target. Reacquisition is time consuming in software. It adds to the complexity of the tracker circuitry if done in hardware. For targets at the edge of the field of view and at  $19^\circ$  angle of attack, the vibration amplitude at the camera can be 25 percent larger, or  $155 \mu\text{m}$ .

Table 1. Target Vibrations at the Model and at the Camera

Rigid Body  $\pm 0.5^\circ$ , 8 to 50 Hz at  $0^\circ$  Angle of Attack

	Roll	Pitch	Yaw	Units
Target At				
x"	-508	-508	-508 $\pm$ 5.3	mm
y"	-305	-610	-610	mm
z"	$\pm 2.2$	$\pm 2.54$	0	mm
Motion at Camera				
z	$\pm 8.3$	$\pm 9.7$	$\pm 63$	$\mu$ m
y	$\pm 1.5$	$\pm 3.8$	$\pm 5.6$	$\mu$ m

Wing Bending, Target at  $x'' = -508$ ,  $y'' = -610$ ,  $z'' = 0$

	$\Delta z'' = \pm 12.7$ mm 20 Hz	$\Delta z'' = \pm 1.3$ mm 200 Hz	Units
Motion at Camera			
z	$\pm 49$	$\pm 4.9$	$\mu$ m
y	$\pm 19$	$\pm 1.9$	$\mu$ m

The capture range shown in Figure 7, for a 200 x 200  $\mu$ m aperture in the image dissector camera tube, has an assured capture circle of

$$(435 - 200) \times \frac{\sqrt{2}}{2} = 165 \mu\text{m radius.}$$

Thus no need for reacquisition software or hardware is expected.

Should the vibration amplitudes be greater than those presently assumed, the use of a larger aperture will solve the problem at the expense of less tolerance to background light and a greater number of cycles to converge for large offsets.

### 3.4 Image Dissector Camera

The cameras used in this system are modifications of a commercially available image dissector camera and digital interface unit. The hardware tracker is an additional item of electronics. A description of image dissector tubes as trackers is in the Appendix.

**3.4.1 Image Dissector Camera.** - The camera head contains the lens, the image dissector tube, the shielded deflection and focus assembly, voltage divider, and preamplifier. The deflection yoke driver, focus current regulator, high voltage power supply and tracker hardware are contained in an electronics unit located near the camera head and inside the pressure isolation vessel shown in Figure 3. Other items of housekeeping circuitry such as the temperature controller and the digital to analog converters are also located with the camera in the pressure isolation vessel.

The tube used in the camera has a 200 x 200  $\mu$ m sampling aperture. The photocathode is a trialkali type, S-20 on a 7056 glass window.

The camera operates static focus and has 15 bit addressing in both x and y axes. The addressable field of view is 12.5 x 12.5mm. One LSB in the deflection is 0.4  $\mu$ m at the faceplate.

The camera requires +/-15 volts supplied by the digital interface unit located outside the wind tunnel.

**3.4.2 Digital interface unit.** - All communications between a camera and the computer take place through this unit. It decodes the computer commands into operating modes of the camera, tracker, and housekeeping circuitry.

An auxiliary circuit located in the model provides the on/off control of the target LEDs. This circuitry occupies about 500 cm<sup>3</sup> and requires 7-10 watts, most used to light the LEDs.



### 3.5

#### Tracker Characteristics

During this study, a single camera, multi-target, point tracker system was assembled using existing laboratory test equipment and hardware. The camera was a general purpose image dissector camera and its digital interface unit. A computer was programmed to run the camera. The track scan and video signal processing algorithm was written in software. This system contained many of the features that will eventually be incorporated into a stereo electro-optical tracker system. Section 3.8 describes the demonstration of this system that was made at ITT-Aerospace/Optical Division, Fort Wayne, Indiana. This section presents results of various measurements made on the system; measurements made to quantify the performance.

3.5.1 Error detector. - The camera plus tracker logic is a feedback system. The system begins with a target position estimate, measures the error in the estimate, and corrects the position estimate. A key element is the position error detector. In this system it is not one discrete piece of hardware, but rather a term describing the results of scanning the target image and extracting a measurement of its position relative to the track scan. Figure 14 shows the measured value for the normalized error detector function

$$E(x) = \frac{F_1(x) - F_2(x)}{F_1(x) + F_2(x)} \quad \left| \quad y = \text{const} \right.$$

This function relates the measured imbalance in the target brightness samples to a position difference between the center of the track scan and the center of the target. When this distance is sufficiently small, the target position is said to be measured. This curve can also be used to relate the video signal-to-noise ratio to an equivalent position noise. The curve is linear for small position offsets near null. Away from null the slope of the curve decreases. For distances greater than 50  $\mu\text{m}$  from null and up to the limits of the capture range, the slope is near zero.

The slope of the  $E(x)$  curve is shown in Figure 15 and is considered to represent the sensitivity of the error detector. A change in error detector sensitivity is also a change in loop gain of the feedback system. Changes in loop gain carry implications for system transient response and stability. For the purposes of these and other experiments, the loop gain was adjusted for best settling and minimum over shoot near null. This gain adjustment was done in software.

The non-linearity of the  $E(x)$  function for large  $x$  is a nuisance. It slows the convergence to null for large offsets as will be seen later. More troublesome are phenomena which cause the slope near null to change. To assure system stability, the maximum loop gain must correspond to the steepest slope through null. Too high gain or an increase in slope could lead to oscillations about null. After the loop gain is set, subsequent loss of error detector sensitivity leads to increased convergence time.

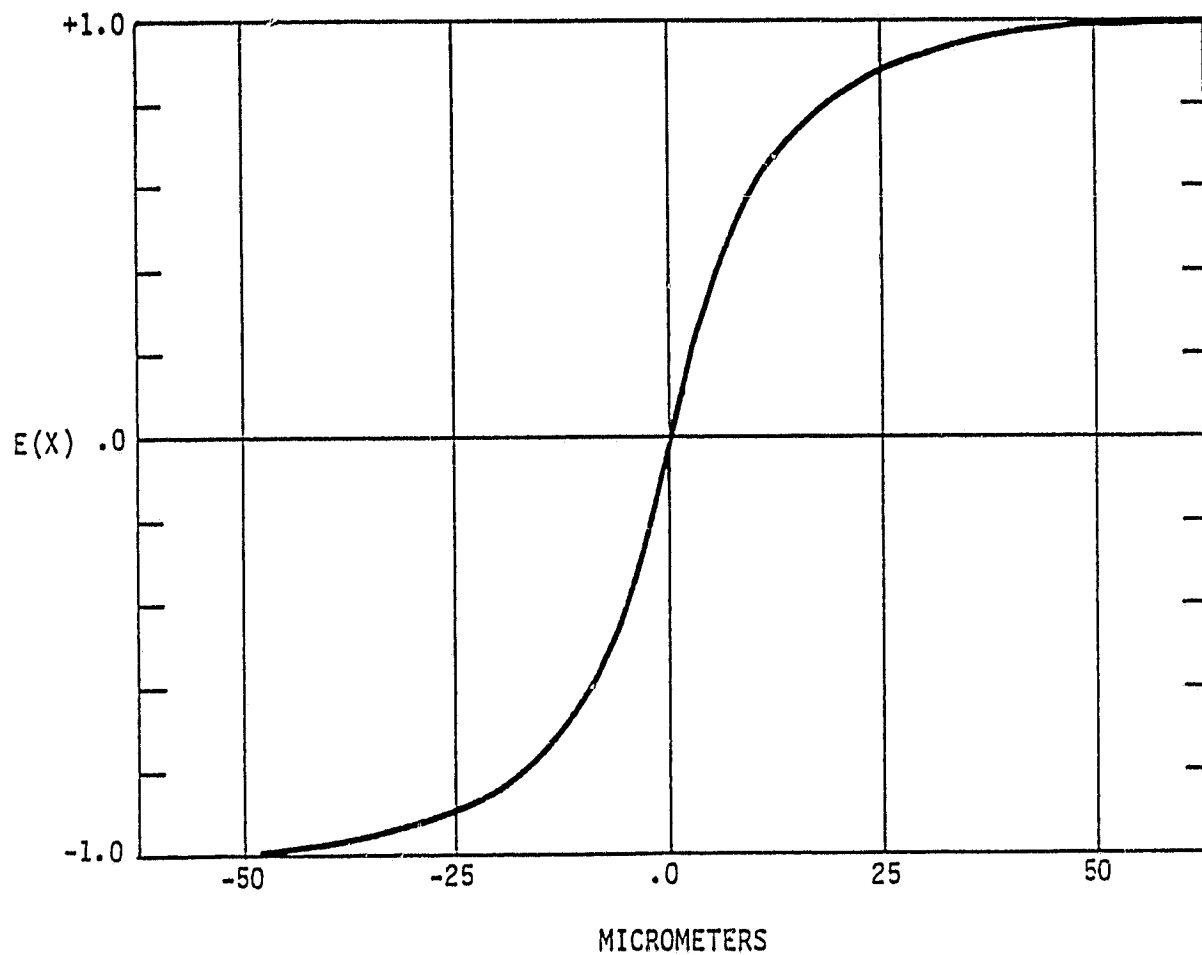


Figure 14. Normalized Error Detector Curve Showing Brightness Unbalance Versus Position Effect.

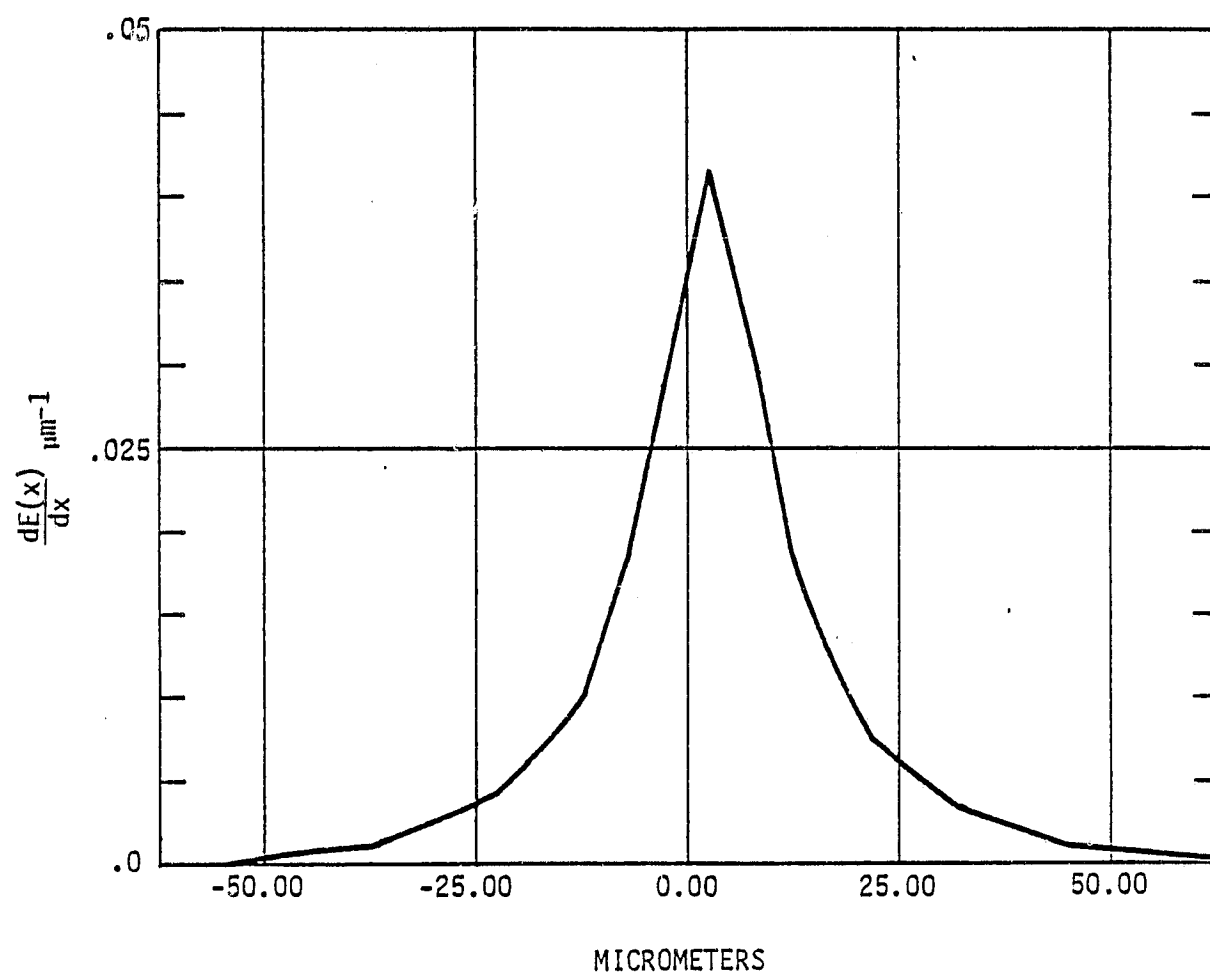


Figure 15. Slope of the Normalized Error Detector Curve

The shape of the error detector curve and consequently its slope near null is affected by changes in the target image. A larger image will cause a reduction in slope. Magnification changes between the model and the camera or depth of focus effects can cause changes in the size of the target image. The design approach has been to make the target image smaller than the optical point spread function and thereby minimizing the magnification effects. The depth of focus effects have been minimized by use of a f/2.8 lens, see Figure 16. A slower lens gives a greater depth of focus but at the expense of target intensity. There is some advantage to creating a larger point spread function. A larger point spread will tend to linearize the  $E(x)$  function over a greater range and thereby reduce the number of cycles needed to converge to null. However, such action requires the optical signal-to-noise ratio be increased in order to hold the same noise equivalent position error.

The targets form an important part of the system design and have an effect upon performance. The experimenter and model builder will need to consider this fact.

**3.5.2 Noise equivalent position.** - Noise equivalent position is a fundamental property of the system relating to measurement precision. It is a way of expressing system noise sources in terms of a single position uncertainty at the faceplate of the camera or at the model. Some of the important noise sources are the shot noise in signal, the D/A and A/D quantization noises, and camera and lens distortions. The effects of vibration and seeing conditions are treated separately under Section 3.6 on accuracy. Camera and lens distortion are presumed to be fixed and measurable.

Figure 17 is a graph of position uncertainty as a function of signal-to-noise ratio of the target signal. The target signal includes both shot noise and A/D quantization noise. The position uncertainty is asymptotic to  $\pm 1/2\text{LSB}^*$  or  $\pm 0.25 \mu\text{m}$ . A signal-to-noise ratio of 30:1 yields a  $\pm 0.5\mu\text{m}$  position uncertainty. This curve resulted from measured performance on the hardware and software used for the demonstration.

**3.5.3 Measurement cycles for null convergence.** - As mentioned in 3.5.1, the error detector function is non-linear away from null. This implies that several track scan measurement cycles are needed. Each cycle contributes, an increment of correction, as the error is nulled to the noise limit.

Figure 18 is a plot of the measured number of cycles needed to converge  $\pm 1\text{LSB}$  or  $\pm 0.5 \mu\text{m}$  of the null position versus the distance from null. The 0 dB gain condition represents no change from the loop gain that provides the fastest settling and minimal overshoot about null. The other curves are deliberate reductions in the loop gain to illustrate the effect upon convergence time. The time to do  $n$  cycles is

$$t_n = (n) 130 \mu\text{s} + (n-1) 40 \mu\text{s}$$

based upon the Figure 8 timing diagram.

\*The demonstration system provided this data and used 13 bit deflection over 4.1 mm or  $0.5 \mu\text{m}/\text{count}$ . The system described in Section 3.4.1 is the one to be used in the tunnel installation. It will use 15 bit deflection over 12.5 mm or  $0.4 \mu\text{m}/\text{count}$ . The signal-to-noise ratio dominates the  $\pm 0.5\mu\text{m}$  position uncertainty.

REPRODUCIBILITY OF THE  
ORIGINAL PAGE IS POOR

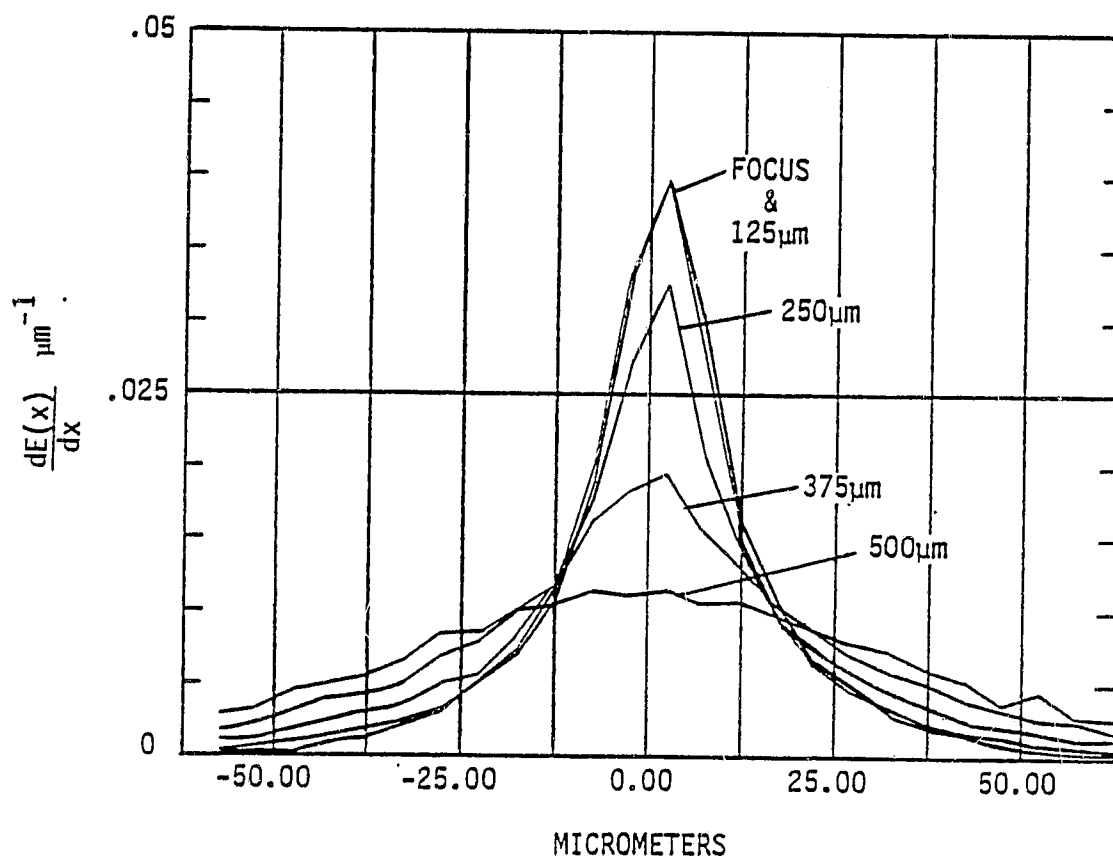


Figure 16. Slope Changes in the Normalized Error Detector Curve for Changes in Focal Plane Position. For an  $f/2.8$  Lens,  $1650 \pm 450$  mm Change in Object Distance Implies  $\Delta \pm 45 \mu\text{m}$  Change in Focal Plane Position.

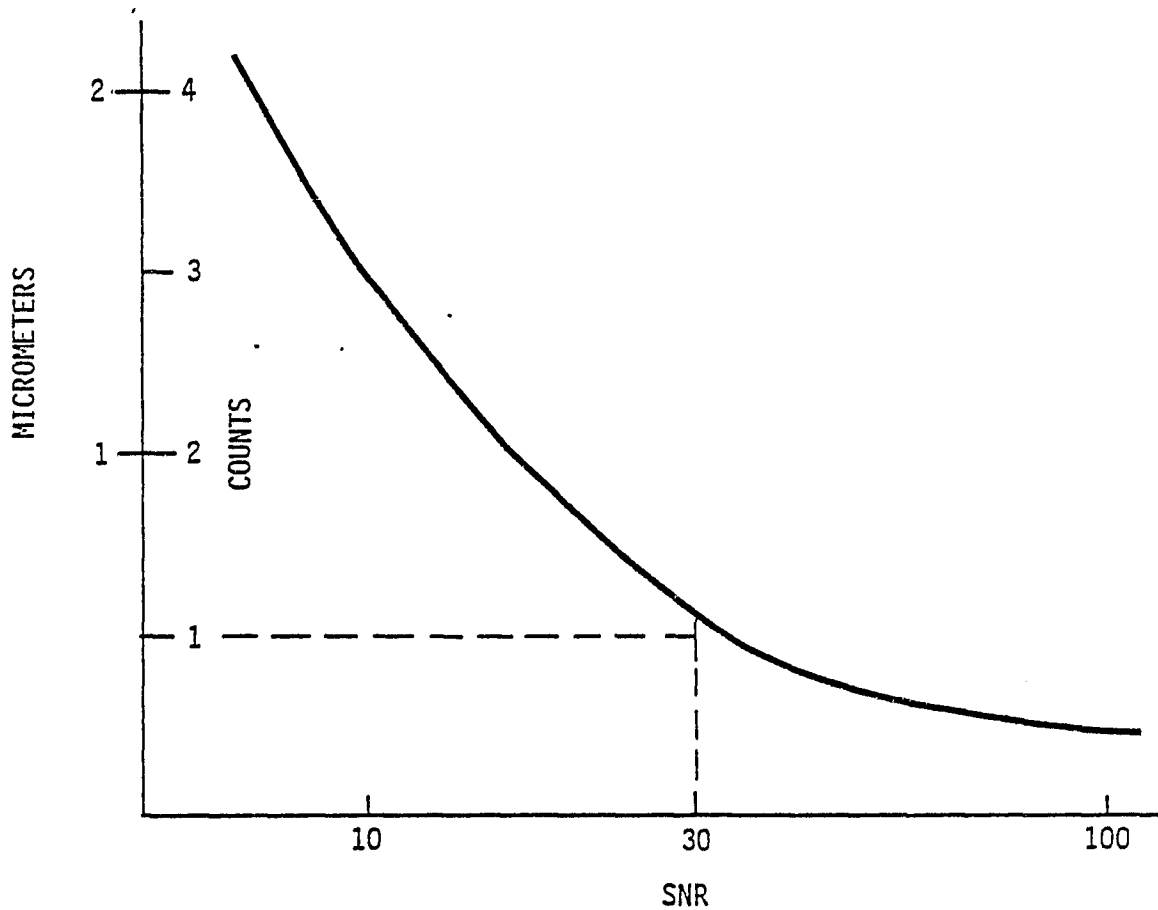


Figure 17. Noise Equivalent Position Versus Signal to Noise Ratio  
(1 Count = 0.5  $\mu\text{m}$ )

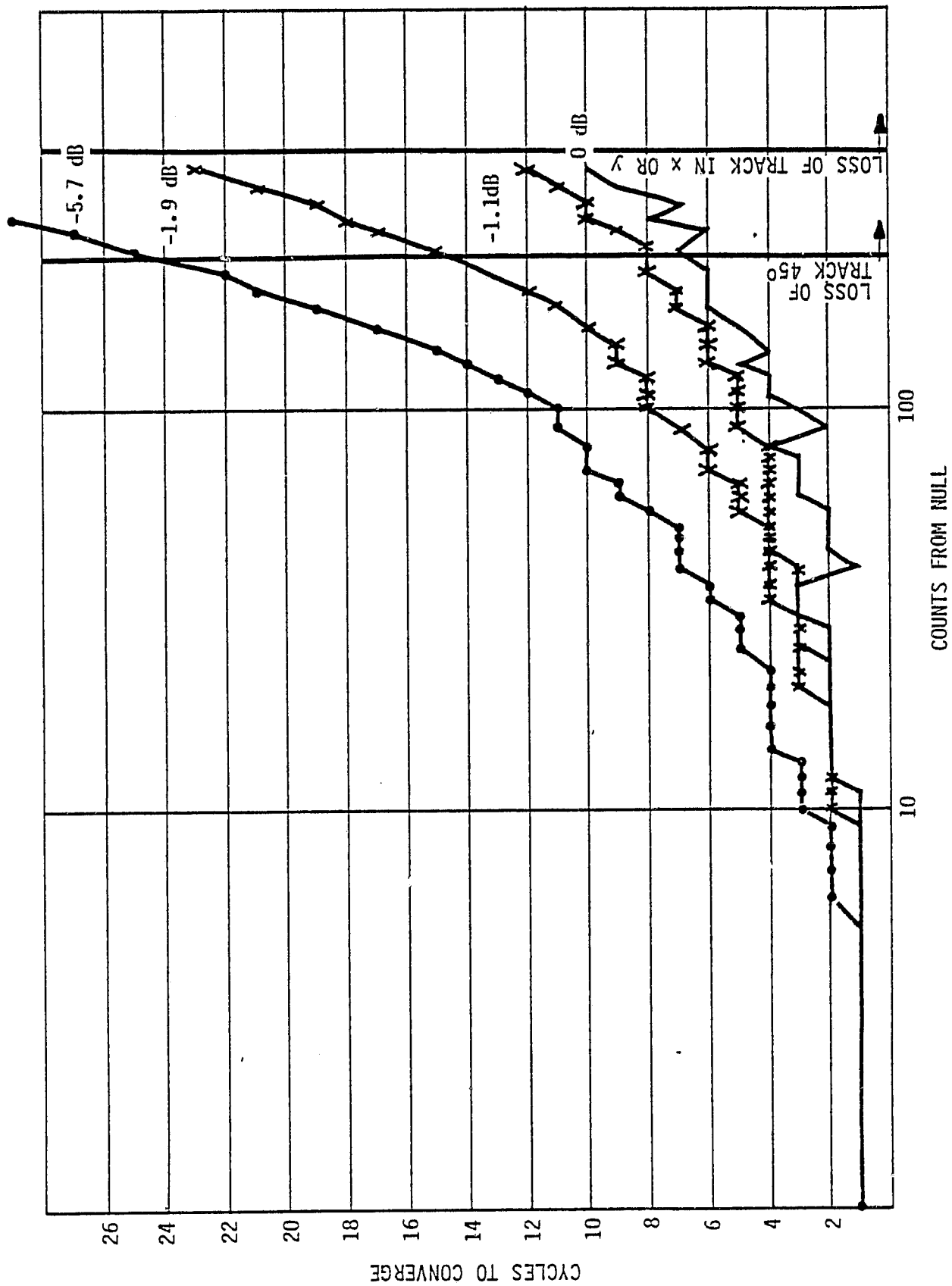


Figure 18. Cycles to Converge to Null Versus Offset from Null and Loop Gain (1 count = 0.5  $\mu$ m)

The stepped, even sawtooth appearance is due to a non-linear change in loop gain implemented in the software tracker used for these tests. When the position correction is calculated to be greater than 20 counts or 10  $\mu\text{m}$ , the correction actually made is 40 counts or 20  $\mu\text{m}$ . This scheme initially overshoots but cuts the number of cycles in half.

Since a target can be expected anywhere within the capture range when the tracker returns to re-examine its position, quite a few cycles could be required to reconverge some targets. Tracker hardware design should allow a degree of adaptation. It should require the target measurement cycles to continue until the correction value is less than or equal to  $\pm 1\text{LSB}$  or until some maximum number of cycles have been executed. This will assure full measurement precision with minimum time expenditure, plus a means to identify less accurate measurements, yet not be trapped forever while attempting to converge high amplitude, rapidly vibrating targets.

### 3.6 System Precision and Accuracy

This section discusses the precision and accuracy of the system concept. Precision is taken to mean the ability to determine small changes in a target position using a stable, repeatable scale of measure; a scale that is consistent throughout the field of view. The accuracy of the system is taken to mean the degree of agreement between the system scale of measure and an external absolute scale such as millimeters at the model. If good system design yields a sufficiently precise system, then a suitable calibration method and data reduction should give a commensurate accuracy.

The limitations upon the precision of the system will be covered by examining the contributions of the several parts. The major divisions are the camera and its lens, the dynamical motions of the targets, the dynamical motions of the camera installation, and the seeing conditions.

Ideally the results should be described in terms of dimensions at the model. However, there is no single factor that relates incremental position changes at the model to image changes at the camera. The relationship depends upon the location of the target in the field of view, the viewing angle of the camera, the focal length of the lens, the range between model and camera, the angle of attack of the model, and vector direction of the position change.

For estimation purposes the model can be considered a flat plate at zero degrees angle of attack, 1650mm range and viewed using a 16mm focal length lens. For a target located at or near the center of the field of view and viewing angles  $(\alpha\beta\gamma) = (125, 90, 35)$  (See Figure 1), the model to image relationship can be described by 3 de-magnification numbers,  $M_x''$   $M_y''$   $M_z''$ .

MODEL SPACE	CAMERA SPACE	FACTOR
$\Delta x'' = \pm 1\text{mm}$	$\Delta x = \pm 8.0\mu\text{m}$	$M_x'' = 125$
$\Delta y'' = \pm 1\text{mm}$	$\Delta y = \pm 9.8\mu\text{m}$	$M_y'' = 102$
$\Delta z'' = \pm 1\text{mm}$	$\Delta z = \pm 5.6\mu\text{m}$	$M_z'' = 178$



3.6.1 Camera and camera lens effects upon system precision. - The camera and lens act in several ways to limit the system precision. The simplest limitation to understand is the one due to small but finite sized deflection increments. The demonstration system, described in Section 3.8, used 13 bit deflection D/A converters over a 4.1 x 4.1 mm field of view. The minimum step size was 0.5  $\mu\text{m}$  at the camera faceplate. The system design concept presented in this report uses a 10 x 10 mm working field of view. Fourteen and 15 bit converters provide 0.8 to 0.4  $\mu\text{m}$  increments respectively while covering a 12.5 x 12.5 mm scanable field of view. Such converters are available for the camera.

D/A converters and cameras have temperature dependencies which affect the size of the area scanned and the stability of the scan center within the field of view. A change in scan size is equivalent to a change in scale factor at the camera faceplate. The magnitude of the error is equal to the distance from the center of the field of view times a  $\pm 20$  ppm/ $^{\circ}\text{C}$  temperature coefficient. Values range from zero at the center to  $\pm 0.12$   $\mu\text{m}/^{\circ}\text{C}$  at the edge of the field of view.

The centering term is  $\pm 10$  ppm/ $^{\circ}\text{C}$  of the full scale size or  $\pm 10 \times 10^{-6} \times 12.5 \text{ mm} = \pm 0.12$   $\mu\text{m}/^{\circ}\text{C}$ . All coordinates within the field of view are equally affected by this factor. The pressure isolation container used to house the cameras must have temperature control because of the  $-195^{\circ}\text{C}$  to  $95^{\circ}\text{C}$  tunnel environment. The temperature coefficients require the control of the temperature, at certain key locations in the container, be the order of plus minus one to two degree Celsius.

The mechanical packaging of the camera and its lens must prevent shifts of the tube relative to the focal plane or coil system. The need is for less than  $\pm 0.5$   $\mu\text{m}$  instabilities, a value consistent with the needs of precision star trackers used for space flight.

The camera and lens both introduce distortions of the field of view. Figure 19 shows the magnified distortion of an uncorrected image dissector camera without lens. It is assumed the lens distortion is comparable or less in magnitude. The dotted boxes are on a 1 mm grid and centered on the true position. The distance from the center to the side of the smaller boxes is  $\pm 25$   $\mu\text{m}$ ;  $\pm 40$   $\mu\text{m}$  for the larger boxes.

This distortion is in principle correctable using a lookup table and interpolating between table entries. A key question is how large must the table be in order to correct  $\pm 0.5$   $\mu\text{m}$ ?

Consider a group of four boxes in Figure 19 whose centers are denoted by A, B, C, D. The distance between AB is 2 mm and the same holds for CD. Assume the x and y position errors are known by measurement for the four positions. The position error for any point E inside the rectangle ACBD can then be calculated by interpolation using

$$\begin{aligned} E_x &= k_1 C_x + (1-k_1) D_x \\ E_y &= k_2 A_y + (1-k_2) B_y \end{aligned}$$

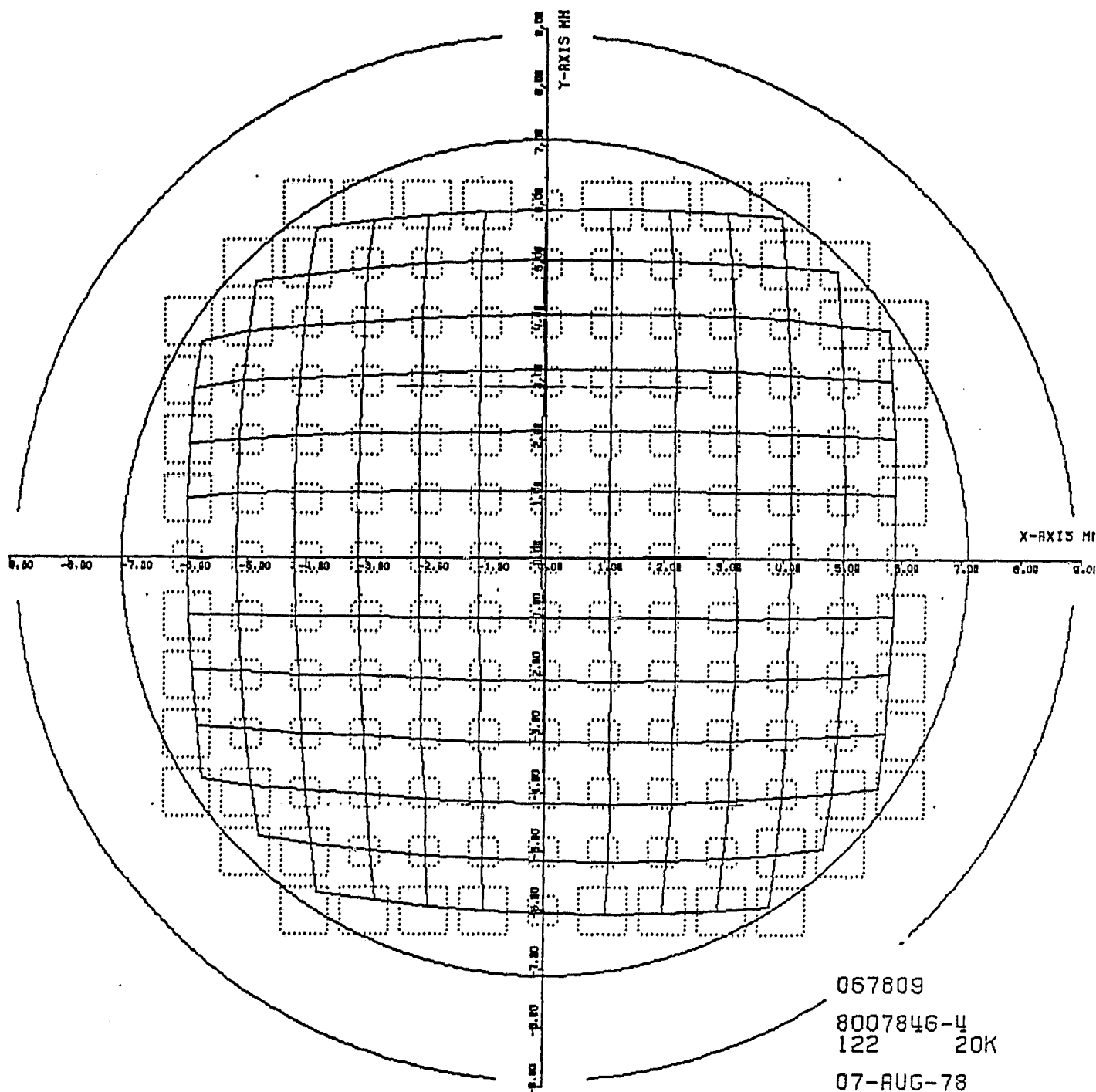
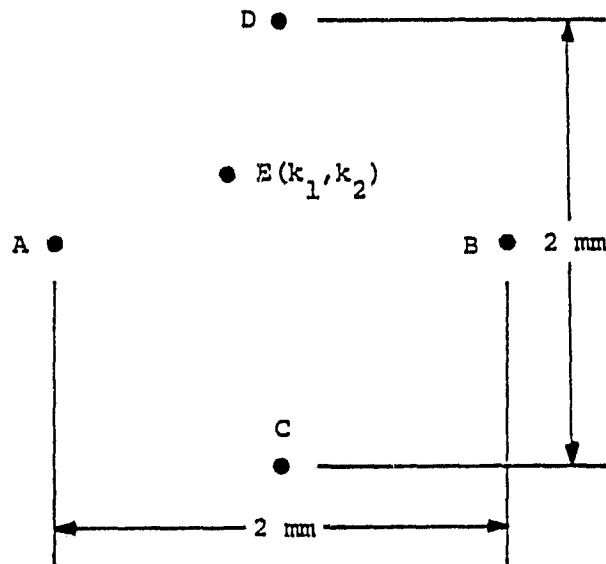


Figure 19. 10X Magnified Camera Deflection Distortion for a Camera Using 25 mm Image Dissector Tube Having a 200  $\mu$ m Aperture



where the subscript denotes the component of the error and  $k_1, k_2$  is the position of point E from C and A respectively. The interpolation is least accurate when E is farthest from the four reference points. This occurs when E is at the center or  $k_1 = k_2 = 0.5$ . E at the center is the case illustrated by Figure 19.

Analysis of the 157 points in Figure 19 showed that  $E_x$  and  $E_y$  calculated by interpolation different from the measured values for  $E_x$  and  $E_y$  by  $\pm 2 \mu\text{m}$  typically and  $\pm 4 \mu\text{m}$  at the greatest.

Assume the interpolation error is proportional to the area of the ACBD cell. Then a  $\pm 0.5 \mu\text{m}$  interpolation error can be achieved using  $(2)^2 \times 0.5/4 = 0.25 \text{ mm}^2$ ,  $0.5 \times 0.5 \text{ mm}$  cell. The  $12.5 \times 12.5 \text{ mm}$  will be mapped to a sufficient density using  $(12.5)^2/(0.25) = 625$  points.

Changes in target light level and background do not directly affect the accuracy as long as a minimum signal-to-noise ratio exists. Section 3.5 shows  $\text{SNR} = 30$  for  $\pm 0.5 \mu\text{m}$  error. A signal-to-noise ratio test is included in the target acquisition routine to ensure sufficient target intensity for the desired measurement accuracy. The SNR test would add about 0.1 second per target to the acquisition time.

In summary the camera, lens and target intensity contributions to the loss of measurement precision are:

Deflection Step Size:	$\pm 0.4 \mu\text{m}$
Temperature Coef of FOV Size:	$\pm 0.12 \mu\text{m}/^\circ\text{C}$ at edge 0 at center
Temperature Coef of Center Offset:	$\pm 0.12 \mu\text{m}/^\circ\text{C}$
Mechanical Package:	$\pm 0.5 \mu\text{m}$
Corrected Lens and Deflection Distortion:	$\pm 0.5 \mu\text{m}$
Signal-to-Noise Ratio:	$\pm 0.5 \mu\text{m}$

3.6.2 Target dynamic motion effects upon system precision. The targets are moving while the cameras attempt to measure their positions. Section 3.3 cited some of the amplitudes and frequencies that might be expected. Figure 20 shows an envelope of possible amplitudes and frequencies for a variety of models. The amplitude is given in  $\mu\text{m}$  at the faceplate of a camera. A scale along the right side shows the number of tracker cycles needed to null a given amplitude offset to  $\pm 0.5 \mu\text{m}$  (Figure 18) and produce a position measurement. Diagonal lines labeled 100g and 200g are lines of constant acceleration at the model. They are calculated using  $g = 4\pi^2 f^2 M_x A / 9800$ ,  $M_x = 100$ . Their purpose is to provide some perspective on the vibration levels being used in the analysis.

The tracker system measurements are time samples of the target position. The objective of the process is to obtain a sufficient number of samples to permit the user to estimate, in a statistical sense, the average target position. The model will be perturbed by random turbulence in the airstream. The turbulence will excite all of the dominant vibration modes of the model and modes of the model-sting combination. The vibrations will be damped and have dominant frequencies but their occurrence depends on the nature of the turbulent input. The time samples of position by the tracking system are assumed to be uncorrelated with the vibration.

There is a period of time called the dwell time  $T$ . During this time the tunnel flow conditions and model angle of attack are held constant. According to NASA, a dwell time of 2 seconds is expected. This finite dwell time sets limits on the low frequency vibrations that the user can tolerate even through the tracker system can quite easily measure positions in the presence of such frequencies. The lower limit is of the order of 1 Hz to 10 Hz.

The time required to make a position measurement is  $130\mu\text{s}$ . An additional  $40\mu\text{s}$  elapses if the same target is repeated or  $70\mu\text{s}$  if a new target is selected. The measurement is actually composed of two  $45\mu\text{s}$  submeasurements separated by a  $40\mu\text{s}$  computation interval. For a target with vibrational motion in a direction  $45^\circ$  to the track scan axes, the x and y position values are taken at slightly different image locations. During the  $85\mu\text{s}$  time interval after x is measured and until y is measured, the x position will have moved at most

$$X = \sqrt{2} A_0 \sin (2\pi f \Delta t)$$

f	$A_0$	X
8	$100\mu\text{m}$	$0.3\mu\text{m}$
20	$100\mu\text{m}$	$0.8\mu\text{m}$
50	$100\mu\text{m}$	$1.9\mu\text{m}$
200	$10\mu\text{m}$	$0.3\mu\text{m}$

These errors go to zero as the motion becomes parallel to the scan axes, leaving the residual errors described for the camera and optics in Section 3.6.1.

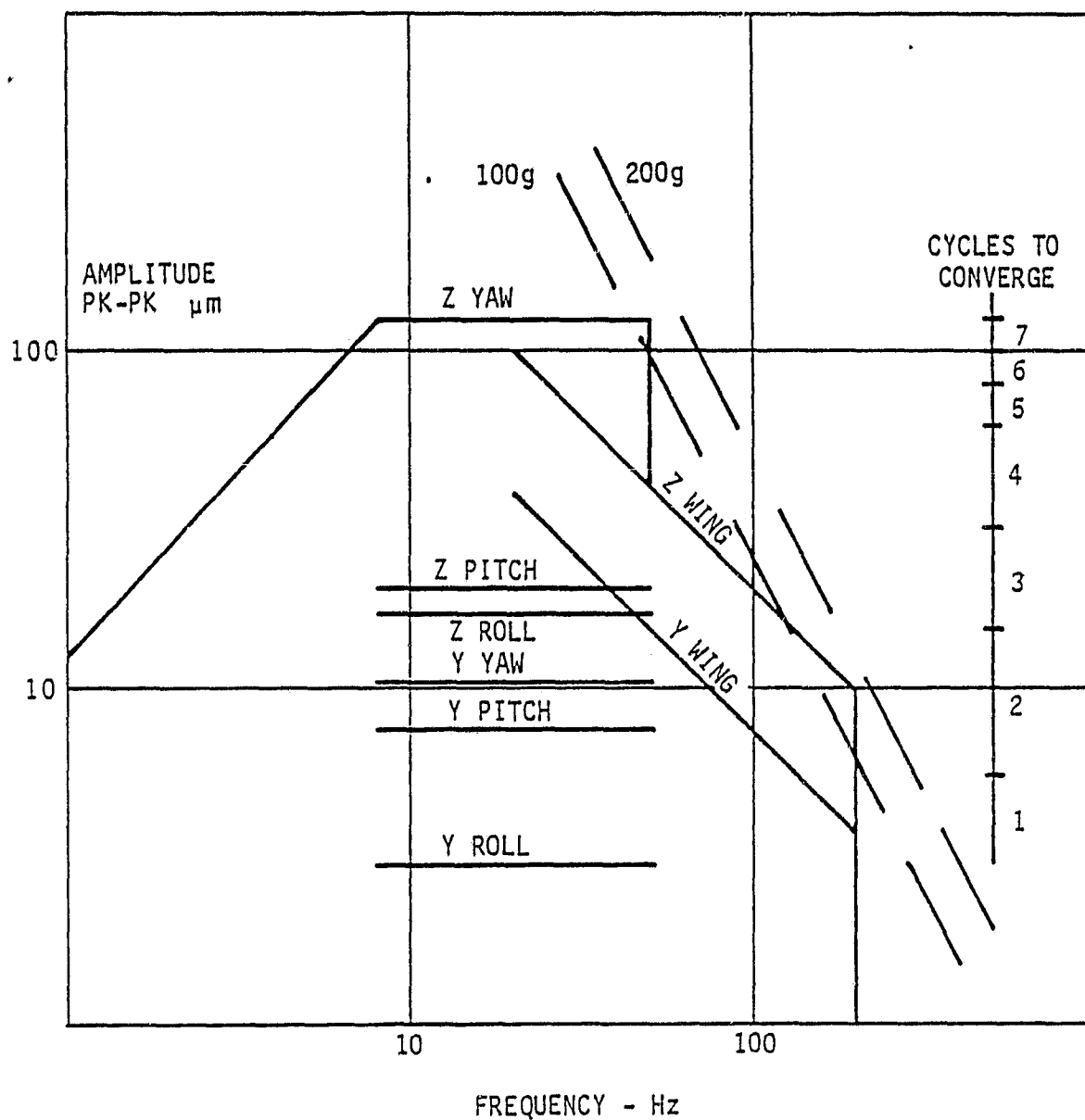


Figure 20. Vibration Amplitude Versus Frequency Spectrum for Some of the Possible Vibration Modes of the Wind Tunnel Model

So far it has been shown that the vibrational amplitudes are within the system capture range, that the measurement is made in a short time, 130  $\mu$ s and that the various errors and uncertainties at the faceplate are of the order of 0.5  $\mu$ m each.

Several questions still remain. How many targets can the system handle, how does the precision depend on this number, how many measurements of a particular target are made, and what observing strategy should be used.

When sampling a sine wave vibration of frequency  $f$ , two time intervals are important. The first one is  $t(n) = 130 \mu\text{s} (n) + 40 \mu\text{s} (n-1)$  where  $n = 1$ . This is the time used to make a measurement of the vibration amplitude. While  $n$  cycles may be needed to converge to null, it is only the time involved in making the (last) position measurement that is important. In sampling systems this is called the aperture time. The second time interval of importance is  $T(N,n) = Nt(n) + (N-1) 70 \mu\text{s}$ . This is the time between samples where  $N$  targets are scanned and each target requires  $n$  cycles for convergence.

The amplitude response of this sampling process is

$$A = A_0 \sin \frac{(\pi f t(1))}{\pi f t(1)} \cdot \sin \frac{(\pi f T(N,n))}{\pi f T(N,n)}$$

where

$A_0$  is the peak-to-peak vibration amplitude, and

$f$  is the vibration frequency..

The first term,  $\sin(\pi f t(1))/\pi f t(1)$  can be set equal to 1 since for all amplitudes and frequencies shown in Figure 20, its value is greater than 0.998. The argument  $\pi f T(N,n)$  can be rewritten in terms of a normalized number of targets and in a manner showing the dependence upon vibration frequency and amplitude.

Let

$$\pi f T(N_0, n) = \pi$$

$$f T(N_0, n) = f N_0 (t(n) + 70 \mu\text{s}) = 1$$

$$\begin{aligned} N_0 &= \frac{1}{f} \frac{1}{(t(n) + 70 \mu\text{s})} \\ &= \frac{1}{f} \frac{1}{(n(130 \mu\text{s}) + (n-1)(40 \mu\text{s}) + 70 \mu\text{s})} \end{aligned}$$

$N_0$  is a function of frequency and  $n$ , the number of cycles to converge to null  $\pm 0.5 \mu\text{m}$ . The number of cycles  $n$  is, by Figure 18 related to the amplitude of the vibration.

The Figure 21 shows the plot of the normalized amplitude response of the system versus a normalized number of targets. The normalization factor for the number of targets is selected based upon the highest vibration frequency to be measured. Several values are calculated and listed in the top table of Figure 21.

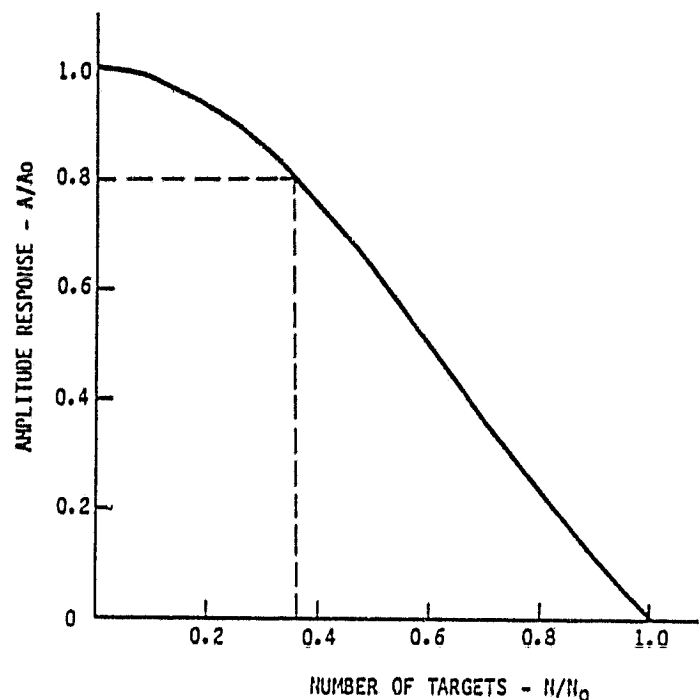
If it is necessary to measure a broad vibration spectrum having large amplitudes and high frequencies, the number of targets will be restricted. The top table and graph of Figure 21 show if  $f = 200$  Hz,  $A_0 = 10$   $\mu$ m and  $n = 2$  cycles to converge, a system using 5 targets will measure an 8  $\mu$ m peak-to-peak amplitude. If the sampling rate and number of targets is selected on the basis of 50 Hz as the maximum frequency, but  $A_0 = 125$   $\mu$ m, the system will measure 100  $\mu$ m peak-to-peak and accommodate three targets. The chief reason for the reduced number of targets is the number of cycles needed to converge. More about that later.

The cases cited have been extreme cases. They permit long term examination of relatively few targets. It is not always necessary to spend all 2 seconds of the dwell time looking at the same 3 or 5 targets. It is only necessary that no more than 3 to 5 high frequency or large amplitude targets be interleaved in the sampling process. At 2700 measurements per second, each of 5 targets has 54 samples in 0.1 second. The other 1.9 seconds could be devoted to other groups of 5 targets, provided the amplitudes of the low frequency vibrations, 1-10 Hz, are low. Should there be concern about the 1-10 Hz content of the vibrations, consider 10 blocks of 5 targets, each block of targets is observed for 0.1 second; a total of 1 second. The 10 blocks are then examined twice for a 2 second total. The point to be made is that the observing strategy depends upon the vibration spectrum. This aspect merits further examination.

If the system is measuring 50 Hz, 125  $\mu$ m vibrations at the calculated 820 measurement per second rate, and if there should be a vibration present whose frequency exceeded 820/2 Hz, the RMS amplitude of this vibration will appear as a noise source added to the various other sources. This aspect of the target position sampling is similar to other sampled data systems. The input signal must be bandwidth limited or else aliasing of the high frequency components occurs which adds to the in-band noise.

The system presented so far has not been completely optimized. Operating conditions have been representative of fast, general purpose image dissector cameras. The tracker algorithm is a very simple one. In Section 3.5.1 it was mentioned that the error detector curve was non-linear. It is this non-linearity that costs most of the system speed at large vibration amplitudes. The tracker is slow to converge to null; seven samples are needed in the case of 125  $\mu$ m offset.

More light at each target allows the linearization of the error detector curve by reduction of slope through null. A 2X reduction in the number cycles needed to converge various offsets seems possible. The lower half of the Figure 21 table is based on such a 2X reduction.



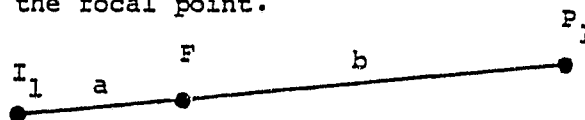
	$f$ FREQUENCY	$A_0$ P-P AMPLITUDE $\mu m$	$n$ CYCLES TO CONVERGE	$1/(t(n) + 70 \mu s)$ MEASUREMENTS PER SECOND	MAX TARGETS $N_0 = \frac{1}{t t_n}$
BASIC SYSTEM AS DESCRIBED	8	125	7	820	51
	20	125	7	820	21
	50	125	7	820	8
	50	40	4	1410	28
	200	10	2	2700	14
SYSTEM WITH REDUCED NUMBER OF CYCLES TO CONVERGE	8	125	4	1410	176
	20	100	3	1850	93
	50	100	3	1850	37
	50	40	2	2700	54
	200	10	1	5000	25

Figure 21. Normalized Amplitude Response Versus the Number of Targets  
Reduced Number of Cycles Assumes 2x more light



3.6.3 Camera dynamic motion effects upon system precision. - For a single camera and small amplitude vibrations, the changes in apparent target position due to camera vibrations cannot be distinguished from changes due to the vibration of the target.

Consider a target at Point  $P_1$ . The vector between the image at the camera and  $P_1$  pivots at the focal point.



Measurement of  $P_1$  in the presence of small amplitude vibrations about  $P_1$  is the purpose of the system. (Small, in this case, is in comparison to the distance between F and  $P_1$ .)

If the target moves a small distance  $\Delta P$  perpendicular to  $FP_1$ , the corresponding change at the image plane is

$$\Delta i = \Delta P \frac{a}{b}$$

where a and b are the magnitudes of  $I_1F$  and  $FP_1$ .

If the camera moves in a plane perpendicular to  $I_1F$  by an amount  $\Delta f$  the focal point F moves. The corresponding  $\Delta i$  change is

$$\begin{aligned} \Delta i + \Delta f &= \Delta f \left( \frac{a+b}{b} \right) \\ \Delta i &= \Delta f \left( \frac{a+b}{b} - 1 \right) = \Delta f \left( \frac{a+b}{b} - \frac{b}{b} \right) \\ &= \Delta f \frac{a}{b} \end{aligned}$$

Equal magnitudes of uncorrelated target or camera motion lead to the same image motion. Therefore target motion plus camera motion must be vector summed and the size of the required capture range determined from the sum.

Magnitudes and frequencies of camera vibrations were unknown at the time of this study. There will however be vibrations.

3.6.4 Seeing conditions. - The light from a target passes through the air flow in the tunnel, an optical window in the wall of the test section, and the window on the pressure isolation container for the camera. All three potentially effect the image quality and the measurement process.

The effects of the windows can be minimized if they are thin flat and not allowed to move relative to the optical axis or camera to model vector. Motions in the plane of the windows have no effect since there is no change in the optical path length or angles of the rays.

Tilts of the windows can be caused by pressure changes, or temperature changes. Tilts of the cameras relative to the window have a similar effect.

For a ray passing through a 10mm thick quartz window at an angle of 35° to the normal, an angular change of +0.5 degree will cause an apparent  $\pm 65\mu\text{m}$  shift in target position at the model. The Figure 22 illustrates this point. Note that the apparent target shift is proportional to the window thickness.

The air in the tunnel also acts as an optical element. Even though the index of refraction is very close to 1.0, the interface at the window has an effect. The wind tunnel static pressure can change from 1 to 9 atmospheres and the temperature from -195°C to 95°C. The index of refraction  $n_t$  of a gas varies as

$$n_t - 1 = \frac{(n_o - 1)}{(1 - 0.00366t)} \frac{P}{760}$$

where  $n_o = 1.000298$  for nitrogen at 0°C and 760mm Hg.

For the temperature and pressure extremes, the  $n_t$  value calculates as

$$n_t (-195^\circ\text{C}, 9\text{atm}) = 1.00937$$

$$n_t (+95^\circ\text{C}, 1\text{atm}) = 1.000221$$

For rays passing at 35° through the 10mm thick window in the test section wall, the change is  $47\mu\text{m}$  in apparent target position at the model. Again this shift is proportional to window thickness.

There is a variation in this window induced error over the field of view since the angle is 35° only at the center. The view changes from 18° to 52° at the edges of the field of view.

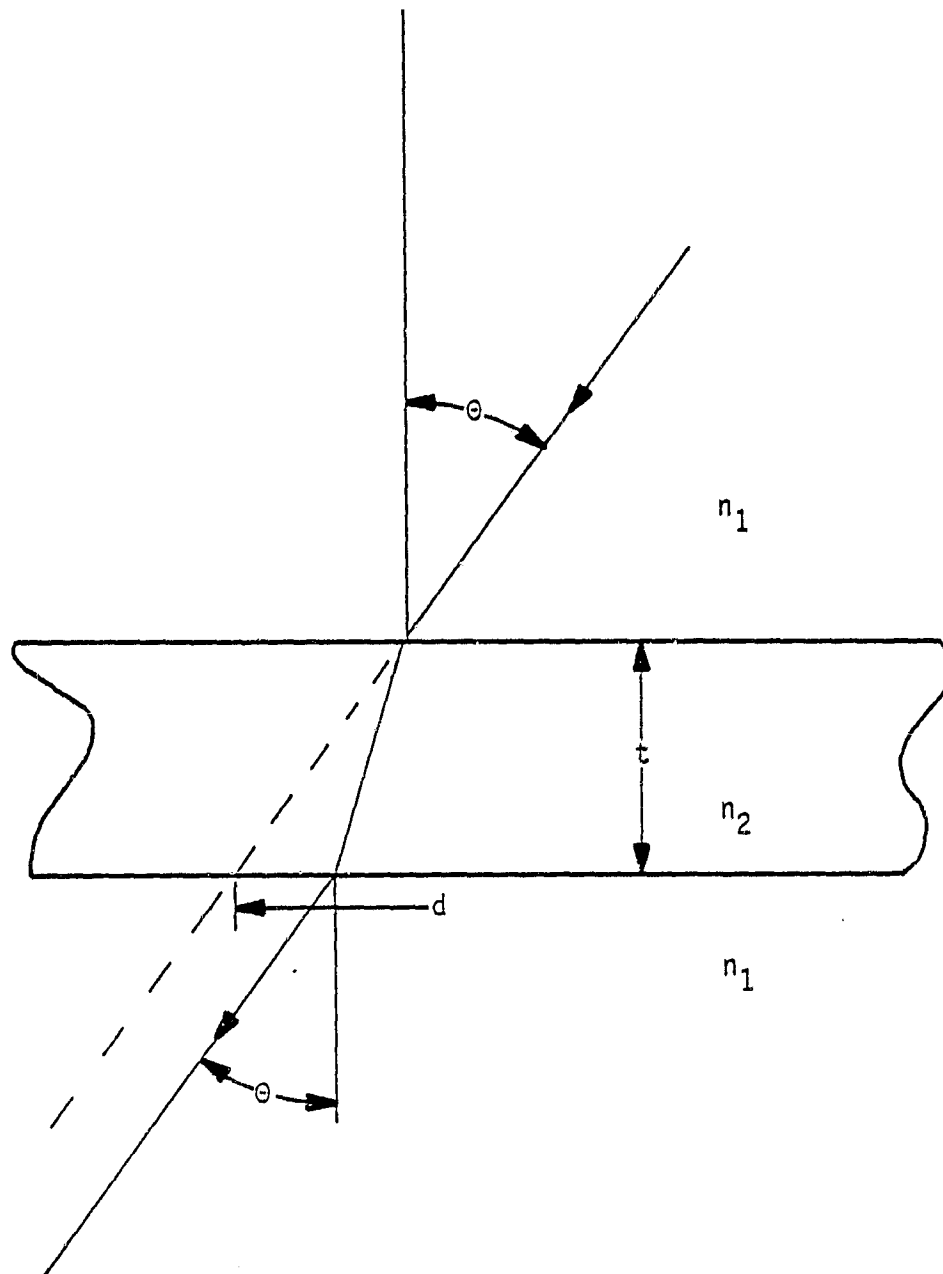
The effects of the temperature and pressure gradients in the vicinity of the test section window and near the model have not been analyzed.

### 3.7 Use of Tracker Cameras for TV Viewing of the Tunnel Interior

Image dissectors were originally conceived and developed for television camera tube use. They have been largely replaced by camera tubes having image storage (vidicons, etc) because of the greater light efficiency of frame storage devices.

Image dissectors are mainly used where slow scan is needed; as in narrowband width image transmission systems. The image dissector signal current is independent of the scan rate. The signal current in storage camera tubes is proportional to the scan rate.

For television purposes, the image dissector camera resolution is set by the aperture in the tube. The nominal size being considered for the tracker system is  $200\mu\text{m} \times 200\mu\text{m}$  square within a field of view of 10 x 10mm square. This results in a TV picture with 100 percent modulation at 50TVL/picture height and zero modulation at 100TVL/picture height; a rather low



$$\frac{d}{t} = \sin \theta \left[ \frac{1}{(1 - \sin^2 \theta)^{1/2}} - \frac{n_1}{(n_2^2 - n_1^2 \sin^2 \theta)^{1/2}} \right]$$

$n_1 = 1.000298$  FOR NITROGEN AT  $0^\circ\text{C}$ , 1 ATM

$n_2 = 1.46$  FOR QUARTZ

Figure 22. Refraction at Test Section Window

resolution image. The typical closed circuit TV resolution of 250TVL/picture height at 50 percent modulation can be achieved with an aperture 50 x 50 $\mu$ m square. Based upon the analysis of the tracker system, it is doubtful that the tracker would work using a 50 $\mu$ m aperture; the capture range would be severely reduced.

Multi-aperture image dissector tubes have been built in the 25 and 44mm sized tubes. There is no basic reason that a dual aperture version of the 17mm tube could not be built. If one of the apertures is 50 x 50 $\mu$ m while the other is 200 x 200 $\mu$ m, the needs of the TV and tracker modes could both be satisfied. However, it can be shown by the following calculation that the TV mode must be slow scan, minutes per frame; or else require high tunnel illumination, 1000ft cd.

The highlight signal-to-noise ratio of a TV picture is required to be at least 35:1 RMS. At this level the image will begin to show noise breakup. The signal-to-noise ratio of an image dissector camera in the TV mode is proportional to the square root of the number of photoelectrons passing through the aperture in a time  $t = 1/2BW$ ; BW = video bandwidth.

$$I_{\text{pixel}} = \frac{e_K \text{ SNR}^2}{\Delta t} \text{ amperes}$$

$$e = 1.602 \times 10^{-19} \text{ Coulomb/electron}$$

$$K = 2.5 \text{ noise factor for image dissectors}$$

$$I_{\text{pixel}} = \frac{(1.602 \times 10^{-19}) (2.5) (35^2)}{\Delta t}$$

The time  $t$  is related to the number of pixels in a TV frame and the frame time. Let the 10 x 10mm field of view be scanned by the 50 $\mu$ m aperture in 25 $\mu$ m steps. There are then  $1.6 \times 10^5$  pixels per field of view. Furthermore, let there be a 5 percent allowance for line and frame retrace. The frame time  $T$  is therefore

$$T = \frac{(1.60 \times 10^5) \Delta t}{(0.95)^2}$$

$$\text{or} \quad \Delta t = \frac{(0.95)^2 T}{1.60 \times 10^5}$$

The pixel current is therefore

$$\begin{aligned} I_{\text{pixel}} &= \frac{(1.602 \times 10^{-19}) (2.5) (35)^2 (1.60 \times 10^5)}{(0.95)^2 T} \\ &= \frac{87 \times 10^{-12}}{T} \text{ amperes} \end{aligned}$$

Image dissectors are rated in terms of maximum total photocurrent. The maximum values is 25 $\mu$ A for the 17mm tube.

The total photocurrent is

$$I_{pc} = (1.6 \times 10^5) I_{pixel}$$

$$= \frac{13.9 \mu A}{T} \leq 25 \mu A$$

Therefore, the shortest frame time is about 0.5 second or 2 frames/second. This TV picture will have noticeable flicker for the viewer.

In order to obtain 25  $\mu A$  of photocurrent, the typical 200 A/lumen photocathode needs a light level of 0.125 lumen or 115 ft cd. This is bright. Scene illumination is 4f#<sup>2</sup> greater or 3600 ft cd for f/2.8.

The conclusion is: use a vidicon.

### 3.8 Demonstration

A single camera operating under control of a 16-bit mini-computer was used to demonstrate multi-target position measurement and tracking. The demonstration showed the ability to search and acquire five targets, to track the movement of these five targets while they were moved at a rate and in a manner simulating a change in the angle of attack of a wind tunnel model, and to measure the position of the five targets under conditions simulating the target vibrations described in Section 3.3.

Since the demonstration used laboratory equipment, a general purpose camera, and a tracker function implemented in software, some scaling of the conditions were necessary.

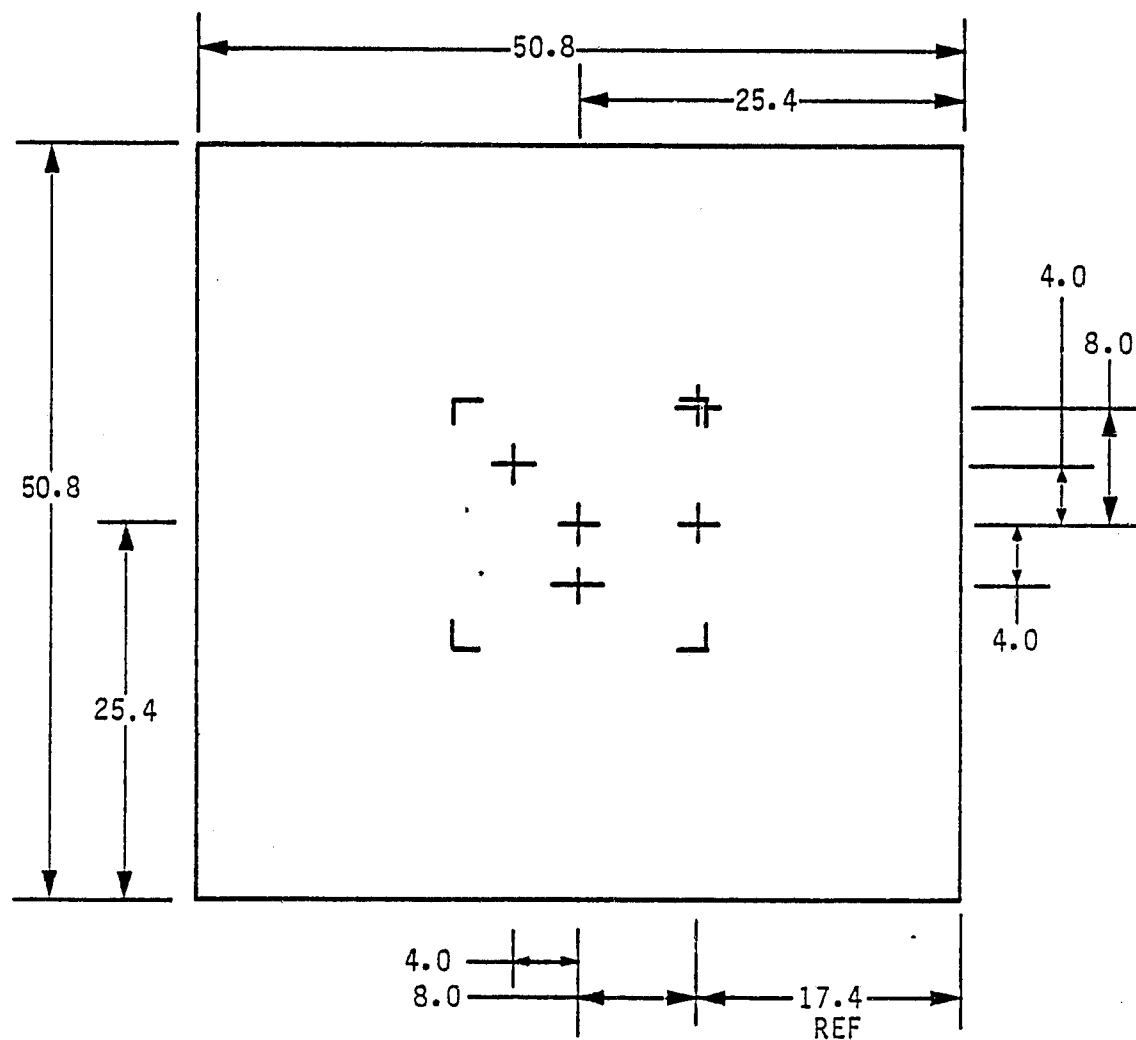
**3.8.1 Field of view.** - The demonstration field of view was 4 x 4mm compared to the desired 10 x 10mm. The smaller field of view was selected in order to achieve 0.5  $\mu m$  deflection increment using the available 13 bit D/A converters. Use of a 15 bit converter permits the entire 10 x 10mm field of view to be utilized at 0.4  $\mu m$  deflection increment.

**3.8.2 Targets.** - The five point targets were pinhole apertures in a metal plate. The targets were back illuminated by a tungsten light source. The image of the test pattern was demagnified onto the faceplate of the image dissector camera using a 55mm f/2.8 lens. The background brightness was minimized to avoid the added task of writing a background suppression routine in the target acquisition software. (See Section 3.2.3.)

The test pattern was mounted on a x/y table that permitted it to be moved about simulating angle of attack changes.

**3.8.3 Target acquisition.** - A program subroutine caused the camera to begin raster scan of the field of view in 50  $\mu m$  steps. If the video signal was above an absolute threshold, the target list was checked for the current coordinate or one within a specific range. If no target was listed, the present one was added. If the target was listed, the scan skipped a safe distance beyond the target and continued until the raster was completed. The time to acquire the five targets was about 5 seconds.

Five 25  $\mu\text{m}$  Apertures at Locations Indicated  
Used with 4:1 Demagnifying Lens



DIMENSIONS IN mm

Figure 23. Demonstration Test Pattern

3.8.4 Track and measurement. Upon completion of the acquisition, the program jumped to the track routine. This routine measured each target position in sequence, updating the target list. The routine was adaptive. It would remain at a target, counting cycles, until the process converged to an operator specified limit or until five cycles occurred. Upon convergence or five cycles the routine moved to the next target.

The adaptive ability allowed the tracker to follow very rapid linear motions of the targets; velocities much greater than would occur during an angle of attack change. This mode assures that no targets would be lost while translating the test pattern rapidly about the field of view.

The tracker action was a time scaled version of the timing diagram shown in Figure 8. Figure 24 shows the comparison between the demonstration of the tracking algorithm. All software was written in FORTRAN to ease the software development task. There is also a sample called display. This was used to show, by means of a 'scope in parallel with the camera, the converged estimate of the target position.

Four time scales are involved. They are shown in Table 2. The five demonstration targets are scanned in a period equal to about 160 targets in the design concept system; or 33:1 ratio.

3.8.5 Target dynamic simulation. - A subroutine was used to generate a table of vibrating target position versus time coordinates. The amplitudes and frequencies used are given in Table 3. The frequencies were scaled to present the same time scaled motion to the demonstration system as the actual frequencies would present to a real time system.

The table of vibrating coordinates was then used to disturb the target coordinates contained in the target list before the target coordinates were sent to the tracker. This creates the illusion that the target has moved since last examined. The tracker then must reconverge to the null position.

Of the conditions listed in Table 3, the tracker occasionally experienced difficulty with the third one, the yaw vibration of  $126\mu\text{m} \times 10\mu\text{m}$  at 50 Hz. Using the 125x rule, this corresponds to  $15\text{mm} \times 1.3\text{mm}$  at the model. It was not clear if this was a dynamic limit or some unresolved problem with the demonstration hardware. The  $126\mu\text{m}$  is inside the capture range.

Table 2. Comparison of Stereo Electro-Optical Tracker System Time Scale with the Demonstration System Time Scale

	Demonstration System	Stereo E-O System
Sample Time	200 $\mu\text{s}$	20 $\mu\text{s}$
Cycle Time	2600 $\mu\text{s}$	130 $\mu\text{s}$
Intercycle Time	2900 $\mu\text{s}$	40 s/70 $\mu\text{s}$
TOTAL for 3 cycles at 1 target	18.1ms	540 $\mu\text{s}$

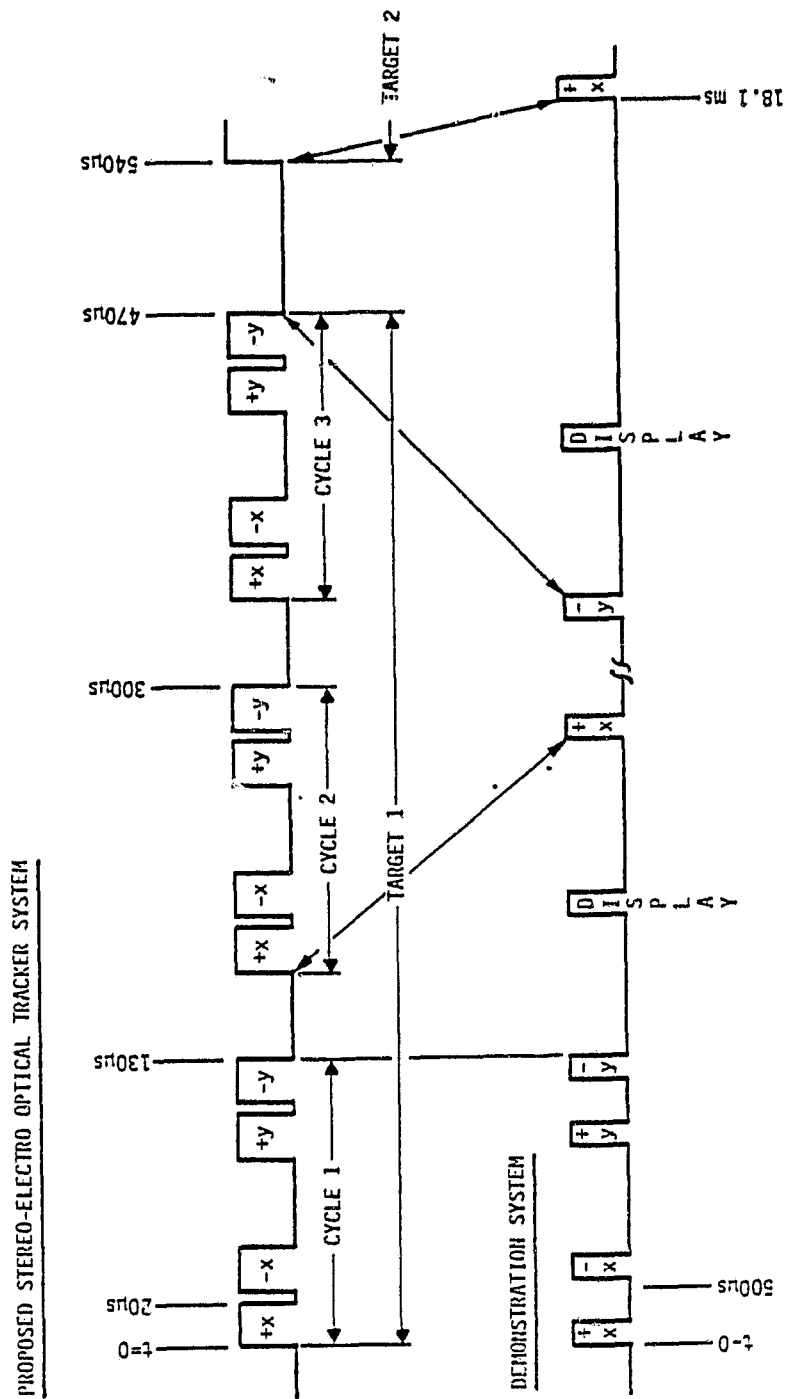


Figure 24. Comparison Between Timing Diagram of Stereo Electro-Optical Tracker System and Laboratory Demonstration System



TABLE 3. VIBRATION SIMULATION FREQUENCIES AND AMPLITUDES

EXTREMES ARE

1. PITCH:	13.4 $\mu$ M 3.0 $\mu$ M	50 Hz
2. ROLL:	25.7 $\mu$ M 7.7 $\mu$ M	50 Hz
3. YAW:	126.0 $\mu$ M 10.0 $\mu$ M	50 Hz
4. WIND DYNAMIC:	78.0 $\mu$ M 38.0 $\mu$ M	20 Hz
5. WIND DYNAMIC:	7.8 $\mu$ M 3.8 $\mu$ M	200 Hz

ALL DIMENSIONS ARE PEAK-TO-PEAK AT THE PHOTOCATHODE.

This study and report provides an analytical and experimental basis to support the concept of a stereo electro-optical tracker system to measure multiple targets attached to aircraft models in the wind tunnel at the National Transonic Facility. The study showed given 0.8m x 1.0m field of view and 150  $\mu$ m precision at the model, 5-50 point targets can be acquired and tracked. Furthermore, the intensities of the targets, tunnel background illumination, and system data rates are within reasonable bounds. A demonstration showed a time scaled simulation of a five target tracker operating at the expected electro-optical signal-to-noise ratio and desired precision. The analysis and demonstration also showed that targets vibrating at frequencies of 8, 50, and 200 Hz can be located and measured. There is a trade among the number of targets per second, the vibration amplitudes, target brightness and contrast that must be considered.

Several important areas remain to be examined or specified. It is these areas that introduce an element of risk to the development and use of this system concept.

Targets and their attachment to the model are critical to the success of this concept. This study proposes that LEDs embedded in the model be used. An alternative is fiber optic light pipes, ends polished flush with the model.

The effects of the distortions in the camera and camera optics on accuracy needs examination from the viewpoint of the stereo-optic transformation. These distortions can be corrected; but knowledge of the required degree of correction for all sources is needed,

The seeing conditions between the target and the model are important. Do the shock waves, turbulence and other pressure gradients degrade the accuracy of the system?

System calibration needs further examination. The study has considered only some of the basic aspects and the general approach.

Lastly, it will be important to know what kind of a thermal and vibrational environment the cameras will experience inside the tunnel pressure vessel. This need is not just for questions of mechanical packaging. Vibrations will contaminate the measurement process. The study shows the system can measure vibrating targets on a vibrating model. System speed and number of targets depends strongly on the vibration amplitudes and frequencies. What are the limits on camera-to-camera and model-to-camera motion. How does the user/experimentor extract useful information about true target position from the three dimensional vibrationally perturbed data recorded by the system.

#### 4.1 Credits

The writer has found this concept of a stereo electro-optical tracker system a most facinating one to examine. The help of David Gray of NASA Langley was most appreciated. He answered many questions about the tunnel environment and didn't mind repeated requests for vibration data. The software for the demonstration was written and debugged in about three weeks time by Doug Renselle of SCS, Inc. His contributions greatly aided the demonstration.

## APPENDIX

The Image Dissector as an Optical Tracker

## APPLICATION NOTE E16

# THE IMAGE DISSECTOR AS AN OPTICAL TRACKER\*

### 1.0 INTRODUCTION

Although the image dissector was probably the first all-electronic optical scanning device to be used (Ref. 1) for generating a video television signal, its first reported use (Ref. 2) as an optical tracking device did not occur until 1960. Since that date it has enjoyed a steadily increasing popularity as a specialized optical scanning device, especially for tracking star (Ref. 3) and laser (Ref. 4, 10) images.

### 2.0 BASIC PRINCIPLES

To understand why the image dissector is so well adapted for optical image tracking, consider first its mechanical analogy shown in Figure 1a. In this mechanical analogy an opaque mask with an aperture is moved in the plane of an image, until the desired image flux falls through the aperture and onto a suitable detector, such as a photomultiplier tube. By determining the precise mask position at which this aperture penetration occurs it is then possible to determine the position coordinates of the image.

More importantly, perhaps, from the standpoint of image dissector operation, once the image is located, its subsequent motion can be tracked by starting a series of small incremental motions of the aperture, without the necessity of continuously, and inefficiently, scanning the total viewed field. It is this ability of the image dissector to adapt its own scanning motion to that of the image to be tracked, which distinguishes it from the majority of other optical trackers.

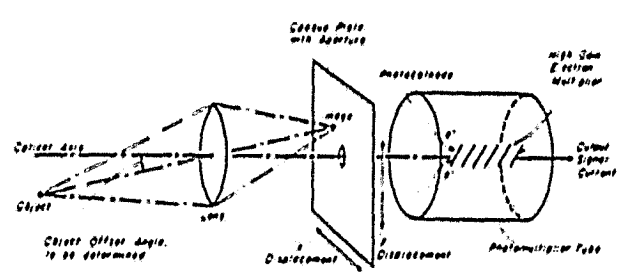
The electronic image dissector shown in Figure 1b can perform exactly the same function as the mechanical dissector, only much faster and without backlash. In this case, the optical image is converted first to an electron image, by a suitable combination of photocathode and electron lens. The electron image is then moved, in a nearly inertialess manner, over a fixed mask containing an aperture. Behind the aperture is a high gain electron multiplier which converts each entering electron into a large, often individually detectable (Ref. 5) burst of charge in the dissector anode circuit.

### 3.0 TYPICAL IMAGE DISSECTOR DESIGNS

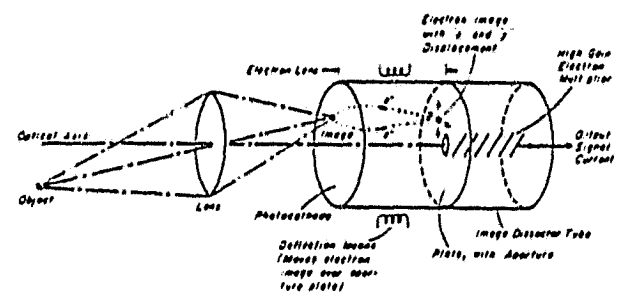
Commercially available image dissectors vary primarily in the methods selected to focus and deflect the electron image, as well as in the diameter of the input optical image which can be accommodated. Figure 2 shows the basic configuration used in three popular types of image dissectors.

\* Paper presented by E. H. Eberhardt at the Optical Tracking Seminar of the Society of Photo-Optical Instrumentation Engineers, El Paso, Texas, January 18-20, 1971.

REPRODUCIBILITY OF THE ORIGINAL PAGE IS POOR



(a) Mechanical Image Dissector



(b) Electronic Image Dissector (Principal Advantages: Low inertia, no gear or bearing backlash)

Figure 1: MECHANICAL AND ELECTRONIC IMAGE DISSECTORS

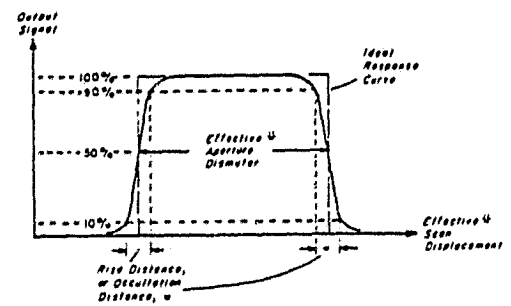
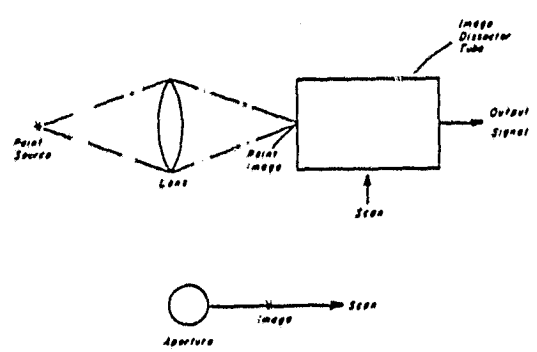
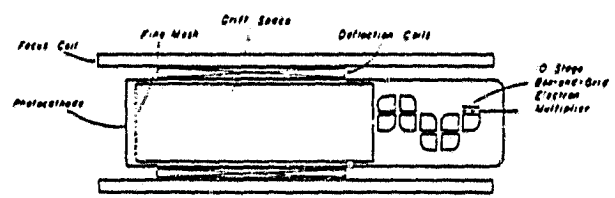
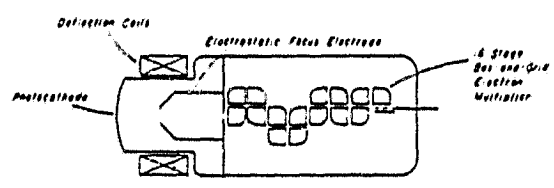


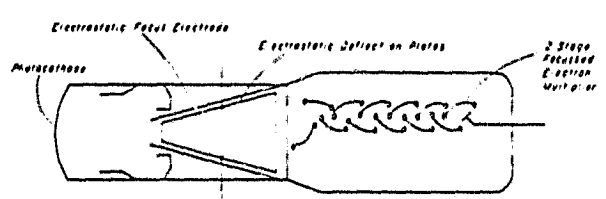
Figure 3: OCCULTATION CHARACTERISTICS



(a) All-magnetic Image Dissector, with Drift Space (dissector type) Examples: F4010, F4011, F4012, F4032 (ITT)



(b) Hybrid Image Dissector (Star Tracker type) Examples: F4018, F4019, F4020, F4021, F4022, F4023, F4024 (ITT)



(c) All-electrostatic Image Dissector, with Deflection Electrostatic Deflection Plates. Example: Reconatron (CBS)

Figure 2: TYPES OF IMAGE DISSECTORS

At the top, Figure 2a, is a Vidisector<sup>®</sup> (Footnote 1), image dissector, an advanced version of the earliest, magnetically focused and deflected dissectors. A fine pre-acceleration mesh is used in close proximity to the photocathode, to accelerate the photoelectrons up to their full velocity as quickly as possible, followed by an electric-field-free drift and deflection space prior to the defining aperture plate. This tube is designed to operate satisfactorily in the same type of magnetic focus and deflection coils used for vidicons and image orthicons. Such an image dissector was used as a star tracker in the first X-15 experimental aircraft (Ref. 6). Its properties as a star tracker have been described by Ostroff and Romanczyk (Ref. 7).

In Figure 2b is shown the basic configuration of a hybrid image dissector with electrostatic focusing and magnetic deflection. This type of dissector, often called a "star tracker" tube, was used in the first reported dissector tracker (Ref. 2) and in other, more recent trackers (Ref. 8, 9, 10), including the star trackers used in Aerobee rockets and on the Lunar Orbiter spacecraft (Ref. 3).

In Figure 2c is shown the basic configuration of a Reconotron all-electrostatic image dissector which was used as an azimuth star tracker on the Mariner series of spacecraft (Ref. 11).

#### 4.0 PERFORMANCE CHARACTERISTICS OF IMAGE DISSECTORS

##### 4.1 Rise (or Occultation) Distance

When a small, "point-source" optical image is focussed onto an image dissector, as indicated in Figure 3, and a linear deflection signal is applied, the aperture can be made to move (Footnote 2) across this point source image, generating a pedestal-like output signal. Ideally this signal should have a sharp rise and decay characteristic, as indicated by the dashed lines in Figure 3 as the aperture occults the point source image. In practice, the rise and decay characteristics are somewhat rounded, with the degree of rounding conveniently describing the capabilities of a particular image dissector. Quantitatively, the rounding can be measured in terms of the aperture displacement,  $w$ , measured at the photocathode, necessary to change the output signal between the 10% and 90% response points, as indicated. The magnitude of the resulting rise distance, or occultation distance,  $w$ , is an important operational characteristic of an image dissector.

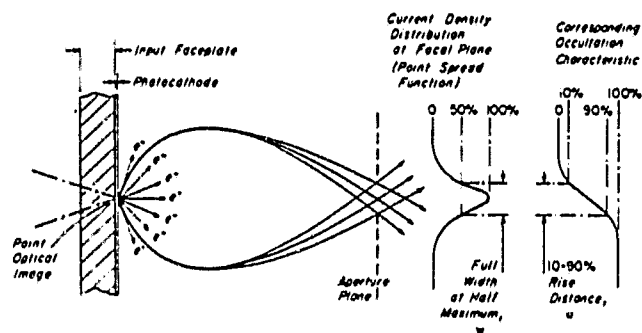
Figure 4 shows how a finite rise distance is generated internally within an image dissector. The group of photoelectrons emitted from a point image on the photocathode, exit from the photocathode with a finite spread of energies (commonly averaging about 0.5 eV) and directed at various angles (commonly with an approximately Lambertian distribution). Thus these photoelectrons tend to spread out as they leave the photocathode, progressively destroying the image quality. This tendency to spread is counteracted by the focussing action of the electron lens which brings the bundle of emitted electrons back to a near-point-source size at its focal plane. It can be shown that the width-at-half-maximum of the resulting, approximately Gaussian, beam density distribution at the image plane is approximately equal to the 10%-90% rise distance,  $w$ . Thus, there are four essentially synonymous terms for the parameter,  $w$ , at focus, namely:

$$w = \text{beam width} = \text{beam diameter} = \text{rise distance} = \text{occultation distance}$$

Figure 5 shows what the total electron beam profile actually looks like in Vidisector image dissectors, for a point source input, and three possible magnetic focus conditions, namely: one loop, two loops and three loops of focus. Focus at the aperture can be assured by choosing a combination of the solenoidal magnetic field strength,

1: Trademark, International Telephone & Telegraph Corp.

2: Although the electron image actually scans over a fixed aperture in the image dissector, it is often helpful in describing dissector behavior to talk in terms of the mechanical analogy, where the aperture is moved over the optical image.



$w$  = Occultation Distance Full Width at Half Maximum  $\approx$  Rise Distance

Figure 4: RELATION BETWEEN THE POINT SPREAD FUNCTION OF THE ELECTRON BEAM AND THE RISE DISTANCE,  $w$ .

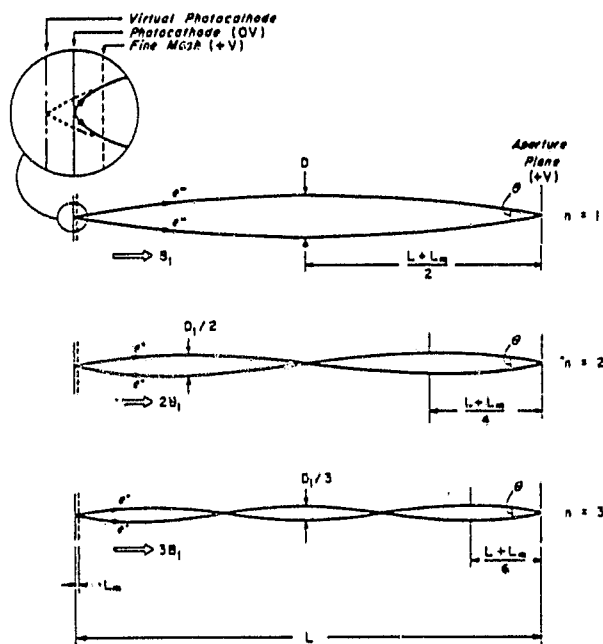


Figure 5: BE-M LOOP SHAPES IN VIDISSECTOR IMAGE DISSECTORS (SHOWING FIRST THREE "LOOPS" OF FOCUS)

$$B_n \approx \frac{2\pi n}{L+L_m} \left( \frac{2mV}{e} \right)^{\frac{1}{2}} \quad D_n \approx 0.53 \frac{L+L_m}{n} \left( \frac{V_{r0}}{V} \right)^{\frac{1}{2}}$$

$$W \approx 1.23 L_m \left( \frac{V_{r0} V_{r10}}{V} \right)^{\frac{1}{2}} \quad \tan \theta/2 \approx 0.83 \left( \frac{V_{r0}}{V} \right)^{\frac{1}{2}}$$

REPRODUCIBILITY OF THE ORIGINAL PAGE IS POOR

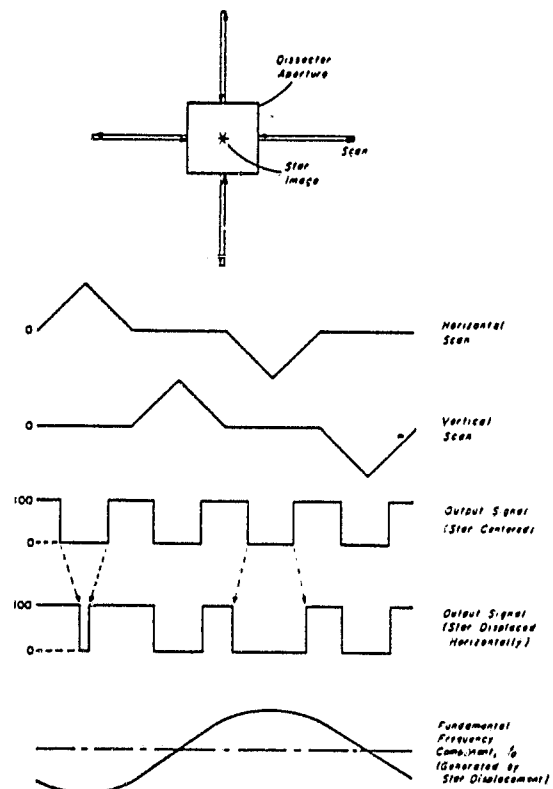


Figure 6: TYPICAL ROSETTE-SCAN STAR TRACKER MODE



$B_n$  in webers/meter<sup>2</sup>; the photocathode-to-mesh voltage,  $V$ , in volts; the photocathode-to-aperture spacing,  $L$ , in meters; the photocathode-to-mesh spacing,  $L_m$ , in meters; and the charge to mass ratio,  $e/m$ , of the electron, in coulombs/kg, such that the following equation is satisfied:

$$B_n = \frac{2\pi\eta}{L + L_m} \frac{2\text{ mV}}{e}^{1/2} \quad (1)$$

Insofar as both the electric and magnetic fields are uniform, and the aberrations introduced by the non-uniform deflection fields can be ignored, the beam width,  $w$ , at focus is given by:

$$W \cong 1.23 L_m \frac{(V_{ro} V_{zo})^{1/2}}{V} \quad (2)$$

where  $V_{ro}$  is the average radial emission energy component of the photoelectrons, and  $V_{zo}$  is the average axial component, in electron volts.

For a typical Vidisector image dissector, such as an F4052, with  $L = 22.5$  cm,  $L_m = 0.32$  cm,  $V = 600$  volts and  $2 V_{ro} \cong V_{zo} \cong 0.3$  eV (white light input to a multialkali photocathode), Equation 2 yields a value of 1.4 micrometers for the beam width,  $w$ . This is approximately 0.003% of the total image field diameter which can be scanned in such a tube (4.2 cm), illustrating the excellent limiting "resolution" characteristics which can be achieved. Measured rise distances as short as 2-5 micrometers, have actually been observed in an F4052 image dissector camera.

The maximum (off focus) beam diameter,  $D_n$ , and the beam convergence angle,  $\theta$  (useful in estimating depth of focus) are given in Vidisector image dissectors by:

$$nD_n \cong 0.53 (L + L_m) (V_{ro}/V)^{1/2} \quad (3)$$

$$\tan(\theta/2) \cong 0.83 (V_{ro}/V)^{1/2} \quad (4)$$

#### 4.2 Possible Tracking Modes

One type of simplified "rosette" scan which can be used (Ref. 2, 3) for tracking a star or laser image with a dissector is shown in Figure 6. Here one applies successively, a small positive horizontal aperture displacement and return, a small positive vertical aperture displace and return, etc., as shown, with the star image initially known to be located somewhere within the aperture area. If the star image is centered within the rest position of the aperture, the output signal, as illustrated, will be a uniform symmetrical series of pulses, of rise distance,  $w$ .

On the other hand, if the star is displaced, the output pulses will become asymmetrical in width, generating a fundamental component of the scan "frequency",  $f_o$ , whose amplitude is linearly proportional to the offset displacement of the image, and whose phase determines the direction of the displacement (see Figure 6). This type of simple, but efficient star tracker, combined with mechanical gimbaling to keep the stellar image within the viewed aperture area has been used (Ref. 3) to track stars within less than 1 micrometer displacement accuracy at the photocathode. For a particular optical system used, this was equivalent to better than 10 arc seconds tracking accuracy. Note that the tracking information, to a first approximation is independent of the magnitude of the rise distance,  $w$ , and of the magnitude of the stellar flux,  $F$ , (assuming that the magnitude of the  $f_o$  frequency component is referenced to the magnitude of the  $2f_o$  component). If so desired, the electronically generated image offset information can be converted to a "DC" centering deflection displacement of the aperture. The aperture can then be made to electronically follow the motion of the star image within the field of view.

Four other possible tracking scan modes are shown in Figure 7. The first, Figure 7a, illustrates the azimuth-only type of tracker used in the Mariner spacecraft (Ref. 11). This tracking mode takes advantage of the fact that a long narrow, slit-shaped aperture can be built into the image dissector tube, with line scan permitting azimuth position information to be extracted without regard to the elevation of the star image.

Figure 7b is a similar tracker, using an L-shaped aperture. Here, both azimuth and elevation information for a star image (or images) can be generated by use of a corresponding L-shaped scan.

Figure 7c illustrates a somewhat more complex type of image dissector tracker. In this case a small aperture is rotated, or wobbled, with a small amplitude, such that image irradiance gradient information is generated. The center of the scan can then be made to move electronically at right angles to this gradient. The dissector then automatically traces out equal irradiance level contours. Such a scheme has been used in an eyeball tracker (Ref. 12) for tracking the pupil of the eye.

And finally, a rather sophisticated image dissector tracker can be constructed whose internal aperture can be adjusted electronically to a specific shape, such as the letter, "A", illustrated in Figure 6d. When such a custom-shaped aperture is then scanned over an image field, it will generate a large, sharply defined, "correlation spike" whenever it crosses precisely over an image area of the same shape. This sharp correlation spike can be used (Ref. 13, 14) with great effectiveness to track complex image shapes against a non-uniform background.

If so desired, dissector tubes may be supplied with multiple apertures, each with its separate read-out electron multiplier, for special optical tracking applications (Ref. 15).

#### 4.3 Signal-to-Noise Ratio

Usually, only one type of random noise is encountered in image dissector trackers, namely the inherent statistical fluctuations of the photoelectrons emitted from the photocathode. Dark noise, i.e., random residual noise generated by the tube itself, and by the external amplifier circuits, in the absence of input flux, is nearly always negligible. This is a direct benefit of the large ( $> 10^5$ ), nearly-noise-free charge amplification present in the electron multiplier of the image dissector.

To calculate the expected magnitude of the photoelectron noise and show how it limits the ability to find and track images, it is convenient, and especially instructive of image dissector behavior, to assume that the dissector scans by making a series of discrete image intensity samples. In this sampling process, illustrated in Figure 8, the scan stops on each aperture-sized element for a short time,  $\Delta t$ , called the dwell time. It can then make a "count" (Footnote 3) of the total number of photoelectrons collected by the aperture.

When only a uniform background irradiance is incident on the photocathode, the resultant output count,  $n_b$  will be given by

$$n_b = L a S_b E \Delta t \quad (5)$$

---

3: While the image dissector can actually count individual output anode pulses corresponding to individual photoelectrons entering the aperture, it is more usual in practice to accumulate these anode charge pulses and generate an average output current.

REPRODUCIBILITY OF THE  
ORIGINAL PAGE IS POOR

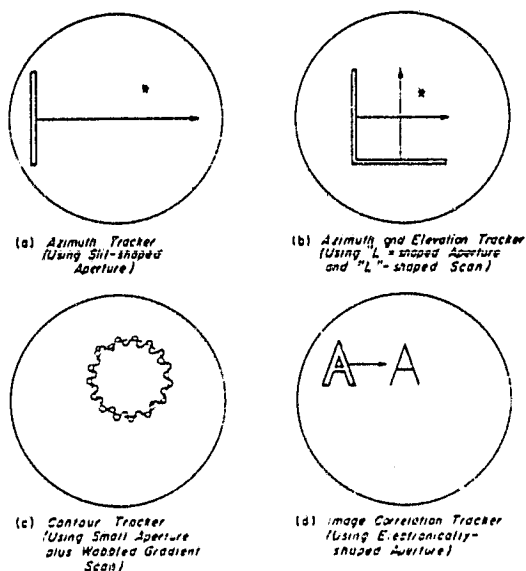
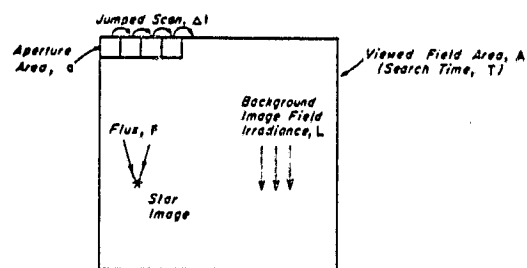


Figure 7: SOME ADDITIONAL IMAGE DISSECTOR TRACKING MODES



$$\text{Background "Count"} = L \cdot A \cdot S_p \cdot E \cdot \Delta t$$

$$\text{Background "Count" Variance} = \text{Noise} = (L \cdot A \cdot S_p \cdot E \cdot \Delta t)^{\frac{1}{2}}$$

$$\text{Signal "Count"} = F \cdot S_i \cdot E \cdot \Delta t$$

$$S/N \text{ Ratio} = (\text{Signal "Count"})^2 / (\text{Background "Count" Variance})^2$$

$$= \left( \frac{F^2}{L} \right) \left( \frac{S_i^2}{S_p^2} \right) E \left( \frac{\Delta t}{A} \right) = \left( \frac{F^2}{L} \right) \left( \frac{S_i^2}{S_p^2} \right) E \left( \frac{T}{A} \right)$$

Figure 8: S/N RATIO DERIVATION, USING JUMPED SCAN  
( $S_p$  = Photocathode Responsivity,  $E$  = Electron  
Multiplier Counting Efficiency)

where

L = background irradiance, incident on the photocathode in (flux units)  $\text{m}^{-2}$  (Footnote 4)

a = aperture area, in  $\text{m}^2$  (Footnote 5)

$S_b$  = photocathode responsivity ratio, for the background irradiance flux, in  $\text{electrons} \cdot \text{sec}^{-1} \cdot (\text{flux unit})^{-1}$  (Footnotes 4 & 6)

E = counting efficiency of the electron multiplier, in output counts per emitted photoelectron collected by the aperture area a.

$\Delta t$  = dwell time, in seconds

Of course, if this background-generated count,  $n_b$ , were exactly constant each time it was made it would not interfere, in any way, with the subsequent ability of the image dissector to find image areas of greater or lesser input flux. But it is not, and cannot be constant because of the inherent random emission of photoelectrons. It will therefore have the usual Gaussian variance, or noise content, given by:

$$n_b^{1/2} = (L a S_b E \Delta t)^{1/2} \quad (6)$$

The noise problem in image dissector trackers under these conditions then resolves itself into whether or not an observed change in the count for a particular image element is an accidental change, according to this expected noise variance,  $n_b^{1/2}$ , or whether it is due to true change in the average flux input. For a point image input (i.e., a star or laser image) the increased count, s, due to the incident stellar flux, F, is given by:

$$s = \text{signal count} = F S_f E \Delta t \quad (7)$$

where F = stellar flux incident on the photocathode, in flux units (Footnote 4)  $S_f$  = photocathode responsivity ratio for the stellar flux input, in  $\text{electrons} \cdot \text{sec}^{-1} \cdot (\text{flux unit})^{-1}$  (Footnotes 4 & 6).

Note that the signal count, for this special case where the signal flux is confined to an area smaller than the aperture, is independent of the aperture area, a.

---

4: The units used to measure flux are optional. Photons/second, watts, or lumens, are the three flux units most commonly selected.

5: In order to automatically correct for the sometimes-unknown electron optical demagnification of the electron lens, aperture dimensions are nearly always expressed in terms of their effective magnitude measured at the photocathode surface.

6: The magnitude of the photocathode responsivity ratio, S, in  $\text{electrons} \cdot \text{sec}^{-1} (\text{incident flux unit})^{-1}$ , depends on the flux units selected and on the spectral distribution of the flux input. Methods of computing this ratio for various flux units and various spectral distributions have been described and tabulated (Ref. 16).

An effective signal-to-noise output power (Footnote 7) radio  $\text{SNPR}_{\text{track}}$  for image dissector star trackers can therefore be written down directly as:

$$\text{SNPR}_{\text{track}} = \frac{F^2 S_f^2 E^2 \Delta t^2}{L a S_b E \Delta t} = (F^2/L) (S_f^2/S_b) E (\Delta t/a) \quad (8)$$

The importance of maintaining high stellar flux,  $F$ , high cathode responsivity to this stellar flux,  $S_f$ , and high electron multiplier counting efficiency,  $E$ , is evident from this equation.

However, changes in the dwell time  $\Delta t$ , and aperture area,  $a$ , must be interpreted with care, since there is usually an interdependence between the aperture area,  $a$ , and the dwell time  $\Delta t$ . This can be illustrated for the special case where a square aperture image dissector scans a total field area,  $A$ , in a total search time,  $T$ , with no scan overlap and negligible fly back time. In this special case the ratio,  $\Delta t/a$  equals  $T/A$ , and the signal-to-noise ratio becomes:

$$\text{SNPR}_{\text{track}} = (F^2/L) (S_f^2/S_b) E (T/A) \quad (8a)$$

In this alternative form, and for this scan pattern, it can be seen that the signal-to-noise ratio is independent of the selected aperture area. Thus in certain star tracking modes one is free to choose any desired aperture size, and thus to locate the star image as precisely as needed, without loss of signal-to-noise ratio.

This rather surprising deduction does not hold when the star image becomes comparable to the aperture size, or when the signal is derived from changes in the input fleet density level, as in TV-type scanning, where the signal is linearly proportional to aperture area,  $a$ . For these latter situations, the more conventional signal-to-noise ratio relationships (Ref. 17) will apply.

If a current measuring external circuit with a noise bandwidth,  $\Delta f$ , is used instead of a counting circuit, the dwell time,  $\Delta T$ , is usually replaced by:

$$\Delta t \cong (2 \Delta f)^{-1} \quad (9)$$

and the counting efficiency,  $E$ , by:

$$E \cong k^{-1} \quad (10)$$

where  $k$  is the noise factor (Ref. 18) of the electron multiplier. Counting efficiencies of 0.85 to 0.95 output counts per emitted photoelectron are easily achieved in image dissectors with well-designed first dynode geometry (Ref. 5). This is reduced by the electron transmission ratio of the mesh (typically 0.6 to 0.65) if a mesh is used, as in Vidisector image dissectors, between the photocathode and the first dynode.

---

7: Image dissector signal-to-noise ratios are also often written in terms of the ratio of output signal current to output noise current.

## 5.0 ADVANTAGES, DISADVANTAGES, AND PROBLEMS OF IMAGE DISSECTORS

The optical tracking systems designer, faced with the problem of selecting an appropriate tracking method, needs to know both the advantages and the disadvantages of the image dissector, as well as some of the problems which can arise. Unfortunately most of the important problem areas concern specific tube types, and often specific tube samples, so it is difficult to make generalized conclusions. Nevertheless some useful statements can be made.

### 5.1 Advantages of Image Dissectors

5.1.1 Fast Deflection: The low inertia of electrons allows fast deflection. Limits are more often established by the external deflection circuits, 1  $\mu$  sec jump times between adjacent image elements and 100  $\mu$  sec jump times across a full image diameter have been achieved, and improvements are in progress.

5.1.2 Adaptable Scan: The image dissector can easily be switched on command, from one scan mode to another, e.g. from search scan to track scan or from search scan to contour-tracing scan, or from jumped scan to continuous scan.

5.1.3 High Tracking Mode Sensitivity: When the aperture of an image dissector is actually observing an optical image to be tracked, it enjoys very high effective sensitivity, equal to or better than the best photomultiplier tubes. No difficulty is experienced in counting individual photoelectrons, and the spurious dark count encountered is extremely small (typically a few counts/second or less).

5.1.4 Linear Input-Output: The output from an image dissector is linearly proportional to the input flux over many orders of magnitude. Thus the image dissector can be used as a precision microphotometer simultaneously with scan tracking (Ref. 19). This property is also often useful in deriving optical intensity information for a computer input (Ref. 20).

5.1.5 Wide Bandwidth: The image dissector can follow intensity modulation of the input flux seen by the aperture from DC up to many megahertz. With special electron multipliers this can be extended into the gigahertz region, making the image dissector especially attractive as a dual mode sensor for optical tracking and wide bandwidth optical communications systems (Ref. 4, 28).

5.1.6 No Gear or Rearing Backlash: Since the aperture as well as the deflection and components can be permanently attached to the tube envelope, there are minimal opportunities for boresight offset errors to occur.

5.1.7 Rugged Construction: The inherent simplicity of image dissector construction permits the tubes to be ruggedized. No difficulty has been experienced in meeting the mechanical requirements for rocket and missile launch; in fact at least one image dissector tracker tube has survived an Aerobee rocket crash landing and was subsequently re-used.

5.1.8 Long Life: Dissectors have now been in essentially continuous service for over 30 years. The absence of a short-lived thermionic cathode, used in other TV camera tubes, make this performance possible.

5.1.9 Damage Resistance: The dissector is inherently resistant (Ref. 21) to many types of damage such as momentary flux input overloading, nuclear radiation exposure, accidental over-volting, etc. For example, a Vidisector image dissector in the ATS-F spin stabilized satellite (Ref. 22), has withstood periodic direct solar exposure through a high speed optical system, with no sun-shuttering and with no removal of voltages, for over three years in space without measurable degradation.

5.1.10 Fast Turn-On: An image dissector is ready to go within a few milliseconds, at most, after application of the proper operating potentials.

5.1.11 Wide Spectral Response: Photocathodes for image dissectors can be formed with spectral responses ranging from the far ultraviolet region, to the near infrared (110 nm to 1200 nm).

## 5.2 Disadvantages and Problem Areas

5.2.1 Low Search-Mode Sensitivity: Since the image dissector wastes all image photoelectron information which does not happen to pass through its aperture at any instant of time, it is inherently less sensitive than "storage" type scanning tubes such as the image orthicon and vidicon, for the wide field search mode, where a large number of image elements must be searched before the image to be tracked is located.

5.2.2 Non-uniform Response (Shading, Blemishes, etc.): The input-output responsivity of an image dissector will generally vary, at least by a small amount, from one point to another over the viewed field. If the change is gradual, it is called "shading", with variations within  $\pm 10\%$  or so over the image field being typical. More serious, in many applications, are the rather sharp variations called blemishes which can occur within one or more picture elements. The number and amplitude of these blemishes is often an individual tube-sample characteristic. However, as in other TV camera tubes, blemish numbers can be kept small by proper quality control during tube manufacture.

5.2.3 Off-Axis Defocussing: When a peripheral image element is deflected into the aperture of a dissector, the effective aperture size and shape, and the rise distance,  $w$ , may change. This can be, and commonly is correctable in practice by applying a dynamic focus signal to the tube focus circuits in synchronism with the deflection. Such dynamic focus signals are usually easy to apply. The residual defocussing, after correction, is partially limited by tube design and partially by the external focus and deflection coil design. In Vidisector image dissectors, with custom wound coils, residual rise distances as low as  $3.5 \mu\text{m}$  after dynamic focusing, have been achieved over the full usable input image area.

5.2.4 Off-Axis Distortion: The actual deflection produced by applying a deflection signal is not necessarily identically proportional to the deflection signal. The resulting image distortion is especially serious in electrostatically focused tubes, which are really satisfactory only for near-axis tracking. In magnetically focused Vidisector tubes the image distortion is largely a function of the coil design geometry, with aperture displacements within less than 1% of their linearly predicted position being readily achieved.

5.2.5 Boresight Hysteresis: Although the image dissector has no gear and bearing backlash problems, there can be an equivalent problem introduced by hysteresis in the deflection circuits (failure to reproduce exactly the same aperture position for a given applied deflection signal). In magnetically focused tubes this can be caused by magnetic hysteresis in the magnetic core material or magnetic shielding material. In electrostatically focused tubes it can be caused by electrostatic charging of internal insulator surfaces. With proper tube and coil design these effects can often be reduced to negligible values.

5.2.6 Scan Delay: There can be a finite delay between the time a deflection signal is applied and the time the aperture reaches its new position. This can be due to eddy current losses occurring in the metal parts in magnetically deflected tubes, or to finite insulator charging time in electrostatically deflected tubes. This problem can be especially troublesome in random jumped scanning (not usually encountered in optical trackers) in which the aperture must move very rapidly over large distances and then be suddenly stopped.

5.2.7 Photocathode Fatigue: With continuous intensive current density loading of a photocathode, it is possible to gradually reduce its responsivity, especially in the red region of the spectrum. By proper tube design, this photocathode fatigue can be greatly reduced, with total photocathode emission charge densities ranging up to several coulombs/cm<sup>2</sup>. Barring tube breakage, sudden, catastrophic failure is almost never encountered.

5.2.8 Gain Stability: The high gain properties of electron multipliers make them inherently sensitive to the magnitude of the applied voltage and to small chemical and physical changes in the dynode surfaces. Thus the applied voltage should be regulated, and the temperature held within reasonable limits, such as  $\pm 10^{\circ}\text{C}$ , to achieve stable gain.

## 6.0 SUMMARY

It can be seen that the image dissector is nearly an ideal device for certain optical tracking applications. It can, and does, compete with mechanical trackers in some areas, and in other areas, with more conventional raster-scan-only television camera tubes.



## REFERENCES

1. Farnsworth, P.T., J. Franklin Inst. 218, 411 (1934).
2. Atwill, W., Electronics 23, 88 (July, 1960).
3. Dieters, R.A., Eisenhut, D.R., and Gates, R.F., Electrical Communication 42, 204 (1967).
4. Dixon, T.P., Wyman, C.L., and Coombes, H.D., Navigation 13, 231 (1966).
5. Eberhardt, E.H., Applied Optics 6, 161, (1967).
6. McGarty, T.P. and Nardella, P.C. (M.I.T. Instrumentation Laboratory), Private Communication (1968).
7. Ostroff, A.J., and Romanczyk, K.C., NASA Technical Note TN-D-5281 (June, 1969).
8. Fitzgerald, B.P., J. SMPTE 78, 29 (1969).
9. Product Engineering, p. 40 (December 21, 1970).
10. Lucy, R.F., Peters, C.J., McGann, E.J., and Lang, K.T., Applied Optics 5, 517 (1966).
11. Goss, W.C., Applied Optics 9, 1056 (1970).
12. Merchant, J., Space Aeronautics, p. 92 (February, 1968).
13. Pennix, E., Wright-Patterson Air Force Base Technical Report TR-68-9, (1968).
14. Hawkins, J.K., and Elerding, G.J., Proc. SPIE Computerized Imaging Techniques Seminar, p. VI-1 (June, 1967).
15. Nielsen, R.S., and Ford, M.A., Optical and Electro-Optical Information Processing, Chapt. 26 (M.I.T. Press, 1965).
16. Eberhardt, E.H., Applied Optics 7, 1037 (1968).
17. ITT Reference Data for Radio Engineers, p. 410 (4th Edition, Stratford Press, 1956).
18. Eberhardt, E.H., Applied Optics 6, 359 (1967).
19. Ball, W.F., and Hoag, A.A., Sky and Telescope, p. 22 (January, 1968).
20. Wing, M.E., Electro-Optical Systems Design, p. 54 (Nov./Dec., 1969).
21. Wolff, C., Applied Optics 5, 1838 (1966).
22. Branchflower, G.A., Foote, R.H., and Figgins, D., IEEE Trans. on Aerospace and Electronic Systems, Supplement AES-3, 63 (November 1967).
23. Lucy, R.F., Proc. IEEE 51, 1962 (1963).